Shear-thinning in concentrated rigid fiber suspensions: Aggregation induced by adhesive interactions

S. Bounoua, Elisabeth Lemaire, J Férec, G Ausias, P Kuzhir

Shear-thinning in concentrated rigid fiber suspensions:

Aggregation induced by adhesive interactions

S. Bounoua[1], E. Lemaire[1], J. Férec[2], G. Ausias[2], and P.Kuzhir[1a]

[1]University of Nice-Sophia Antipolis, CNRS UMR7336, Laboratory of Condensed Matter Physics, Parc Valrose, Nice 06100 France

[2]Institut de recherche Dupuy de Lôme (IRDL), University of Bretagne-Sud, EA 4250, LIMATB, F-56100 Lorient, France

Synopsis

This work is focused on shear thinning behavior of suspensions of rigid non-Brownian fibers dispersed in a Newtonian liquid. The work consists in developing a new theoretical model and conducting accurate experimental measurements. The shear thinning is expected to be caused by adhesive interactions between fibers. Experiments on polyamide (PA) fibers (present work) and carbon nanotube (CNT) suspensions [Khalkhal *et al.*, J. Rheol. **55**, 153-175 (2011)] have revealed the following features: (a) the flow curves exhibit a pronounced pseudo-plastic behavior interpreted in terms of the progressive aggregate destruction at the increasing shear rate; (b) the enhancement of the shear thinning with an increasing particle volume fraction is observed and explained by an increase of the strength of effective interactions between particles, as their concentration increases; (c) a weak yield stress of the PA fiber suspensions is detected in a controlled-stress mode and explained by the liquid-solid transition as the concentration of aggregates (constituted by fibers) approaches the close packing limit; (d) the shear thinning is much stronger in CNT suspensions because the adhesive interactions play a more important role between nano-sized CNT particles than between micron-sized PA fibers. A theoretical model considering the coexistence of transient aggregates with free non-aggregated fibers has been developed. The model allows viscosity calculations in terms of the aggregation parameter – the ratio of adhesive to hydrodynamic forces. It captures qualitatively the above-mentioned shear thinning behaviors and fits reasonably well to the experimental data on both PA fiber and CNT suspensions.

I. Introduction

Fiber-reinforced composites are broadly used in civil engineering, automobile and aerospace industries. Fabrication of these materials is often related to extrusion or mixing of fibers dispersed in a liquid matrix [1]. The composites are usually charged with a large amount of particles. Therefore, their successful fabrication and processing require a deep understanding of rheology of concentrated fiber suspensions.

Since the pioneering work of Jeffery [2], the rheology of dilute and semi-dilute fiber suspensions has been well understood and documented, see reviews by Larson [3], Petrie [4].

[a] Corresponding author: kuzhir@unice.fr

In concentrated suspensions, short-range interparticle interactions play an important, if not decisive, role. The effect of short-range hydrodynamic forces and of direct mechanical contacts has been understood through theoretical modeling [5,6] and direct numerical simulations [7–9]. In suspensions of fibers dispersed in a Newtonian solvent and interacting with each other through lubrication forces, direct collisions and Coulombic friction, all these interactions produce a single scaling for the stress, $\sigma \sim \eta_0 \dot{\gamma}$, with η_0 being the solvent viscosity and $\dot{\gamma}$ – a characteristic value of the rate-of-strain tensor (shear rate in the case of a simple shear flow). These suspensions exhibit a viscous behavior with the shear viscosity linear in particle volume fraction φ at low concentrations and nearly quadratic with φ at higher volume fractions [7,8]. The last trend is explained in terms of pair-wise interactions between fibers. Non-hydrodynamic interactions, such as adhesive or electrostatic repulsive forces between fibers, as well as elastic bending of flexible fibers produce non-linear scaling of the shear stress with the shear rate.

From a general perspective, the role of the non-hydrodynamic interactions becomes less important with increasing shear rate. In most cases, this results in a shear thinning behavior. The degree of shear thinning strongly depends on the types of interactions between particles, as well as on fiber flexibility, as discussed below:

1. In purely repulsive systems, the electric double layer may substantially increase the effective particle size and lead to gelation transition and consequently to a yield stress at particle volume fractions well below conventional dense packing fraction [10]. Electrostatic repulsion has recently been found to be at the origin of a yield stress in nanofiber suspensions [11].

2. Excluded volume interactions between rigid or semi-flexible fibers could also lead to gelation of the nanofiber suspension [12].

3. In attractive systems with colloidal nanoparticles, the interplay between the electrostatic repulsion and the van der Waals attraction governs the degree of particle flocculation and yielding behavior [13-15]. At the same time, adhesive interactions produce a moderate shear thinning in suspensions of rigid micron-sized rod-like particles, such as polyamide [16, 17], ceramic particles [18], wollastonite [19].

4. Elastic bending of flexible micron-sized or nano-sized fibers is another mechanism inducing both shear thinning or yield behaviors observed in pulp suspensions [20, 21], carbon nanotube (CNT) composites [22, 23], solutions of agar fibers [24]. The yield stress in flexible fiber suspensions comes from the formation of an entangled network whose strength depends mostly on inter-particle solid friction and, to a lesser extent, on the colloidal forces between them, as revealed by particle level simulations of Klingenberg and co-workers [25, 26]. Theoretical models by Toll and Månson [27] and Servais *et al*. [28] allow a correct prediction of the yield stress in short fiber polymer composites during their forming, while the model of Keshtkar *et al*. [29] captures the transient viscosity of semi-flexible fiber suspensions.

Surprisingly, theoretical modeling of the rheology of rigid fiber suspensions with colloidal interactions is less documented. One of the first rigorous models considering aggregation of rigid fibers has been developed by Ma *et al*. [30], in the case of Brownian fibers. This model introduces a continuous series of fiber populations with different degrees of aggregation. The model captures well the shear thinning behavior and shows a good agreement with experiments on CNT suspensions. However, the role of the colloidal interactions cannot be well understood. First, the shear-induced destruction of aggregates is taken into account only implicitly by the introduction of phenomenological shear rate dependencies of the aggregation and disaggregation rates. Second, the model introduces distinct rotary diffusivities for each population, and these diffusivities are taken to be independent of shear rate. The shear thinning is thus a synergy of the two following effects: (a) the fiber alignment at increasing Péclet numbers; and (b) disaggregation generated by a progressive decrease of the aggregation rate with increasing shear rate. More recently, a multi-scale model of aggregated fiber suspensions has been proposed by the same research group [31-33]. This approach considers both the dynamics of the rod-like particles inside the cluster and the dynamics of the whole cluster. The model allows a precise determination of the cluster rotation and deformation in shear flows. At this moment, colloidal interactions between fibers constituting the aggregates are not explicitly introduced, and the rheology of the clustered suspension is not analyzed in details.

Another model allowing capturing the shear thinning in fiber suspensions has been recently developed by Natale *et al*. [34] and Férec *et al*. [35]. This model discards aggregation of particles and considers short-ranged forces between contacting fibers. The authors capture shear thinning behavior introducing a non-linear lubrication force (proportional to $\dot{\gamma}^n$, $0<n<1$) between fibers that mimics a combined effect of the short-range hydrodynamic and non-hydrodynamic interactions. This force is weighed by the contact probability and affects both the orientation state (producing more isotropic orientation distribution) and the stress tensor. Such a phenomenological approach provides a good agreement with experiments on CNT suspensions. However, the role of the colloidal interactions remains unclear. In our recent work, we have extended this model to van der Waals interactions and solid friction between fibers [36]. Affine motion of the fibers in shear flow has been supposed. Despite the fact that aggregation was neglected, this model predicts a yielding behavior of the suspension with an apparent yield stress being totally defined by the strength of the van der Waals interaction. The model gives a satisfactory agreement with experiments on CNT suspensions at high shear rates, at which both the shear stress and the first normal stress difference are quasi linear with the shear rate and the extrapolation of the flow curves on zero shear rate gives the apparent yield stress. The model does not capture initial rounded shape of the flow curves. This disagreement comes probably from the aggregation of the suspension at low shear rates discarded in the model.

In some rigid fiber suspensions, such as CNTs subjected to moderate shear stresses, the particles experience attractive colloidal interactions often leading to aggregation [30, 37]. It is therefore important to develop an adequate theoretical model for rigid fiber suspensions

with aggregation induced by these interactions. To the best of our knowledge, such aggregation model explicitly accounting for attractive colloidal forces has never been reported in literature for rigid fiber suspensions, even though various cluster models exist for suspensions of spherical particles [3, 38]. Furthermore, the experimental rheological results often depend on the mode of the suspension preparation and on the shear history [39]. Because of relatively large periods of fiber rotation, the steady state of the shear flow is expected to be achieved at a long time usually exceeding the typical duration of standard rheometric measurements. These two factors complicate the comparison between the theory and experiments on steady-state flows. Only accurate experiments ensuring the steady state and independence of shear history could be safely compared to the model.

This allows us to formulate the main objectives of the present work: (a) develop a theoretical model of aggregated fiber suspensions, in which the aggregate behavior and the suspension viscosity would be explicitly expressed through short-ranged adhesive forces between fibers; (b) conduct new rigorous experiments on the steady-state shear flow of non-Brownian fiber suspensions with adhesive interactions and compare these experiments to the theoretical model. The theory proposed in the present work is inspired by the multi-population aggregation model of Vaccaro and Marrucci [40], Ma *et al*. [30], the contact probability approach of Djalili-Moghaddam and Toll [5], Férec *et al*. [6] and a scenario of aggregate rupture under shearing forces developed by Snabre and Mills [41] for aggregated suspensions of spheres. The rheological experiments are made with neutrally buoying polyamide (PA) fibers dispersed in a Newtonian solvent in the range of the shear rates and shear stress when the fibers can be considered as almost perfectly rigid. We test our model on two different experimental systems exhibiting aggregation behavior – PA fibers (the present experiments) and CNT suspensions (experiments of Natale *et al*. [34]).

This paper is organized as follows. The theoretical model is presented in Sec. II. The experimental details are explained in Sec. III. Experimental results are reported and compared to the theoretical model in Sec. IV. Conclusions and perspectives are outlined in Sec. V.

II. Theory

II-A. Basic assumptions and qualitative behavior

Let us consider a steady state simple shear flow of a suspension of fibers dispersed in a Newtonian solvent of a viscosity η_0. The Cartesian coordinate frame is chosen in such a way that the axes x_1, x_2 and x_3 correspond to the flow, velocity gradient and vorticity directions, respectively, as depicted in Fig.1a. The flow is considered to be homogeneous on a macroscopic scale, and the volume average velocity is defined by the vector $\mathbf{v} = (\dot{\gamma} x_2, 0, 0)$, where $\dot{\gamma}$ is the shear rate.

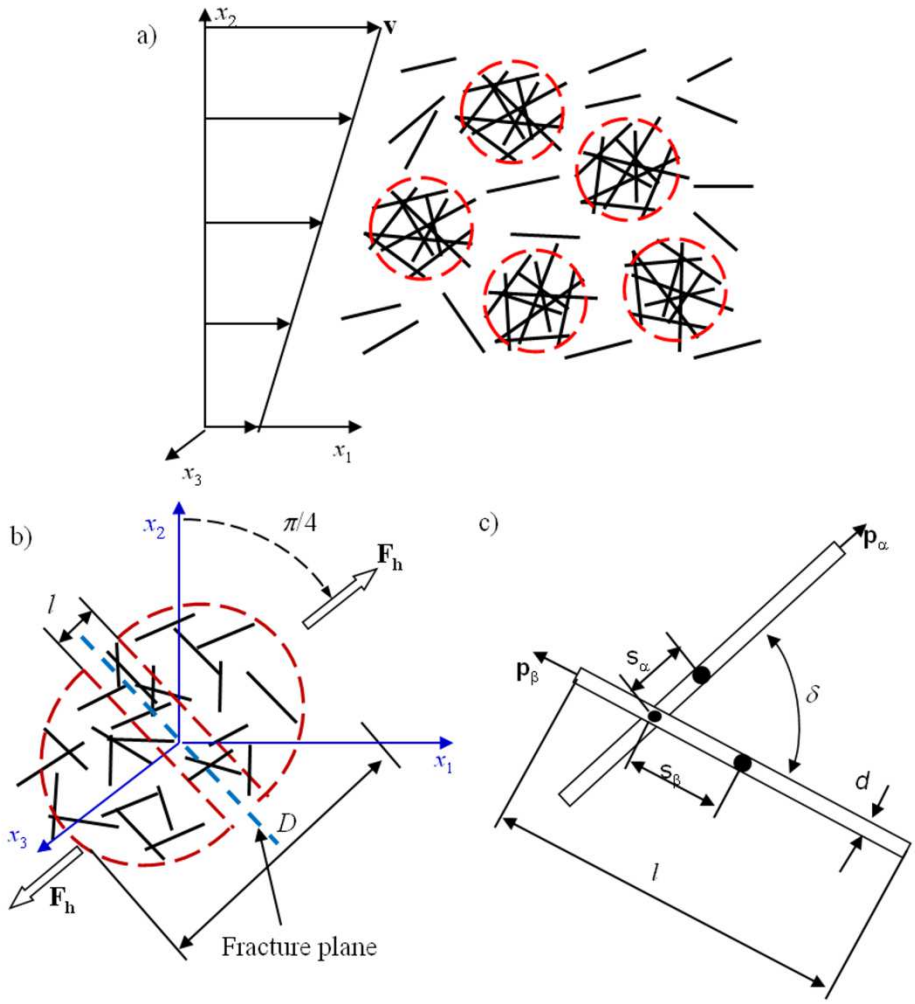

Fig. 1. Problem geometry. The two-population approach is schematically presented in figure (a). According to this approach, the spherical aggregates are dispersed in a suspension (population) of free fibers dispersed in a liquid carrier [cf. assumption (3) of Sec. II-A]. Aggregate rupture in the middle plane is presented in figure (b). Two contacting fibers inside an aggregate are shown in figure (c).

To get the physical insight into the role of adhesive interactions on aggregation and rheology of fiber suspensions, first we present a qualitative picture of the suspension behavior introducing the following simplifications and assumptions:

1. The fibers are considered to be perfectly rigid, non-Brownian and mono-disperse, i.e. all having the same length l, diameter d and aspect ratio $r=l/d$. The high aspect ratio limit $r>>1$ is considered. As it will be stated below, this limit affects the fiber orientation distribution, their contact probability and the suspension viscosity. The gravitational settling of fibers is neglected. The validity of these conditions is checked in Sec. C of Supplemental Materials [42] for the PA fibers.

2. The flow is considered to be laminar both on the scale of the whole suspension and on the scale of the aggregates or isolated fibers. This condition is satisfied by low values of the

Reynolds number, $Re < 1$, at all the scales of the problem, as shown by estimations in Sec. C of Supplemental Materials [42].

3. The model is developed for attractive colloidal interactions which can stick the fibers together and induce spatial heterogeneities as well as their cooperative motion under shear. The cooperative motion of particles can be quantified by a spatial correlation function of particle velocities associated to a certain correlation length [43]. This allows us to define the aggregates as the regions with presumably higher particle concentrations showing a coherent motion of fibers and delimited by a correlation length *D*. The following assumptions are related to the structure of the aggregated suspension:

3.1. As often observed in flocculated fiber suspensions, the aggregates are periodically formed by relative translational and rotational motion of fibers and periodically destroyed by shearing forces – see review by Kerekes [44].

3.2. The whole suspension is considered to be a two population system – transient aggregates immerged in a suspension of free fibers filling the space between them, as depicted in Fig.1a. The fraction of fibers involved into aggregates is denoted by Φ_1, while the fraction of free fibers is Φ_2. The particle conservation implies:

$$\Phi_1 + \Phi_2 = 1 . \tag{1}$$

3.3. In the dynamic equilibrium at steady state, the rates of aggregate construction and destruction are the same; the fractions Φ_1 and Φ_2 remain constant with time and are defined by a kinetic equation formulated in Sec. II-D.

3.4. For the sake of clarity, we will consider aggregates of spherical shape, while extension of the model to elongated shape (prolate ellipsoids of revolution) is developed in Sec. A of Supplemental Materials [42].

3.5. The contribution of aggregates to the suspension viscosity is estimated ignoring filtration flows and relative motion of fibers within the aggregates (rigid aggregate assumption), as if we dealt with a hard sphere suspension of an effective particle volume fraction equal to $\varphi_a = \Phi_1 \varphi / \varphi_i$, with φ - volume fraction of fibers in the whole suspension, φ_i – internal volume fraction of aggregates. Note however, that such viscosity estimation can be subject to some uncertainty because both internal flows and relative motion of fibers may appear during fragmentation of aggregates unless this process is very fast compared to their living time.

3.6. The suspension viscosity is calculated using the Krieger-Daugherty relationship [3], in which the shear viscosity, η_f, of anisotropic free fiber population is used as the viscosity of the suspending medium for aggregates. Perturbation of the orientation state of the free fibers surrounding the aggregates, and its consequence on η_f value are neglected. Studies on the liquid crystalline polymers charged with hard sphere particles show that this approach gives at least a semi-quantitative agreement with experiments for the composite viscosity [45].

3.7. The aggregate behavior (and, as a consequence, the suspension rheology) is governed by the dimensionless ratio of the characteristic adhesive force F_A to the characteristic hydrodynamic force σd^2 (with σ - the applied shear stress):

$$N_A = \frac{F_A}{\sigma d^2}, \tag{2}$$

called hereinafter the aggregation parameter.

4. Two length scales of inter-fiber interactions are considered. The hydrodynamic interactions correspond to a length scale of about a fiber diameter d and to the separation between fibers, $h_R << h_H < d$, where h_R is the surface roughness scale. The adhesive interactions usually have a shorter length scale h_A. Both aggregated and free fibers should experience these two types of interactions. However, adhesive interactions are supposed to be negligible for free fibers. This statement is confirmed by *a posteriori* estimation of adhesive and lubrication forces for free fibers [see Section IV-C, Appendix D]. On the other hand, according to Assumption 3.5, the aggregates contribute to the suspension viscosity through their effective volume fraction φ_a, which is defined by the cohesive strength F_c of the aggregates [Sec. II-C, Appendix A]. For rigid aggregates, F_c is uniquely determined by adhesive forces between aggregated fibers before they begin to slide over each other during aggregate break-up. Thus, the hydrodynamic force between aggregated fibers does not intervene into calculations of the cohesive strength and suspension viscosity.

5. Two different scenarios of the break-up of inter-fiber contacts during aggregate fragmentation are considered: (a) rupture in the direction normal to the contact surface; (b) sliding of fibers along each other. In the case (a), friction does not intervene, and the cohesive strength of the aggregate is fully defined by the normal colloidal force F_n. In the case (b), the cohesion strength is defined by tangential friction force F_τ, while the normal colloidal force F_n intervenes into the cohesive strength through a friction law. The cases (a) and (b) will be hereinafter referred to as, respectively, the normal and the tangential rupture scenarios.

6. The classical Amontons-Coulomb friction law is supposed for the tangential rupture:

$$F_\tau = \mu F_n . \tag{3}$$

Here μ is the friction coefficient, whose typical values vary in a relatively narrow range for polymer fibers in different solvents, namely μ=0.3-0.5, as measured experimentally [46, 47]. Note that little is known about friction mechanics at nanoscale, especially in the boundary lubrication regime. However, the simplest Amontons-Coulomb law still allows correct predictions of the friction between single crystal nanoparticles [48], as well as of flows of concentrated colloidal nanoparticles [49] or hard-sphere suspensions [50].

7. The three following assumptions are related to the internal aggregate structure:

7.1. The orientation state of the fibers inside the aggregates is considered to be isotropic. However, to check whether the orientation distribution strongly affects the aggregate cohesive strength, we extend our model to nearly aligned state and obtain only a slight difference with respect to the isotropic orientation distribution [Appendix A]. Thus, the model can be applied for our experiments with PA fibers showing an intermediate orientation state.

7.2. The internal aggregate structure corresponds to the colloidal glass state, characterized by spatially homogeneous distribution of fibers with a fractal dimension equal to 3. This state occurs within the range of the internal particle volume fractions inside the aggregates, $0.7/r \le \varphi_i \le 5.4/r$, valid for the high aspect ratio limit [51, 52]. The lower bound of this interval corresponds to the percolation threshold. Analysis at the end of Sec. II-C shows that concentration of fibers inside the aggregates in our PA suspensions is above the percolation threshold.

7.3. All the aggregates have the same internal volume fraction φ_i, corresponding to the limit of their mechanical stability [see Sec. II-C].

8. The characteristic aggregate size, *D*, is supposed to be much smaller than the width of the flow channel *b*, and possible wall interactions are neglected. Particle/aggregate migration induced by shear rate gradients or normal stress gradients in rheometric flows are also neglected for both populations of free and aggregated fibers. These both assumptions are *a posteriori* verified, at least, for the PA suspensions [Sec. III-B].

The approach introduced in the assumption (3.5) allows us to calculate separately the viscosity of the free fiber population suspension [Sec. II-B] and then the viscosity of the whole suspension [Sec. II-C]. To close the problem, the unknown fractions Φ_1 and Φ_2 of fibers belonging to both populations will be determined by a kinetic equation in Sec. II-D.

II-B. Viscosity of the free fiber population suspension

The rheology of this population is governed by the fiber-fluid and hydrodynamic fiber-fiber interactions, while adhesive interactions are negligible [Assumption (4) justified in Sec. IV-C]. In what follows, on the basis of our previous work [36], we will briefly describe how the viscosity of the free fiber population can be found accounting for hydrodynamic interactions between fibers.

Only the short-range hydrodynamic fiber-fiber interactions are considered. They correspond to lubrication forces that are assumed to be proportional to the contact surface [53] and to be linear in velocity [5]. For two perfectly smooth cylindrical surfaces (i.e. when the separation h_H between surfaces of free fibers is well above the roughness scale h_R, as confirmed for our PA suspensions, cf. Table IV), the expression for the lubrication force reads [54]:

$$\mathbf{F}_{\text{lub}} = \frac{3\pi\eta_0 d^2 \mathbf{u}}{\left|\mathbf{p}^\alpha \times \mathbf{p}^\beta\right| h_H} \tag{4}$$

where $\mathbf{u}$ is the relative velocity of the approach of two fibers, whose orientation is described by unit vectors $\mathbf{p}^\alpha$ and $\mathbf{p}^\beta$. The gap h_H between free fibers is taken as a free parameter in the model.

The lubrication forces are weighed over the contact probability introduced by Férec et al. [6] and estimated in the high aspect ratio limit, $r >> 1$, using the tube model of Doi and Edwards [55] and taking into account the length-scale h_H of hydrodynamic interactions:

$$dP_H = 2n_2(d + h_H)\left|\mathbf{p}^\alpha \times \mathbf{p}^\beta\right| ds_\alpha ds_\beta \psi_\beta d\mathbf{p}^\beta \tag{5}$$

where n_2 is the particle number fraction in the free fiber population, ψ_β is the angular distribution function of the neighboring fibers β; s_α and s_β are the distances between the contact point and the centers of the fibers α and β [Fig. 1c].

The hydrodynamic interactions between fibers induce their stochastic angular motion [56] that can be mimicked by an isotropic rotary diffusion process with a phenomenological rotary diffusivity

$$D_r = C\varphi\Phi_2\dot{\gamma}, \tag{6}$$

accounting for pair-wise interactions between fibers with frequency proportional to the particle volume fraction ($\varphi\Phi_2$ in the case of the free fiber population) and to the shear rate. The dimensionless constant C accounts for geometrical details of the interaction.

The orientation state of the fibers can be found in low diffusion, $D_r r^3/\dot{\gamma} << 1$, and high aspect ratio, $r >> 1$ limits, following the work of Leal and Hinch [57]. In this limit, the moment $\left\langle p_1^2 p_2^2 \right\rangle$ of the orientation distribution function does not depend on D_r and is equal to $\left\langle p_1^2 p_2^2 \right\rangle \approx 0.315/r_e$, with $r_e \approx 1.24r/\ln^{1/2} r$ being the equivalent aspect ratio of fibers Brenner [58]. The shear viscosity η_f of the free fiber population depends only on the moment $\left\langle p_1^2 p_2^2 \right\rangle$. Thus, η_f appears to be independent of the rotary diffusivity, and the unknown constant C does not intervene into the final expression for η_f.

The stress tensor is obtained by the averaging of the local stress over the contact probability [Eq. (5)] and over the fiber orientation, using the slender body theory for fiber-fluid interaction [59]. The component of lubrication force parallel to the fiber axis gives a contribution proportional to the square of the particle concentration. Since non-hydrodynamic interactions between free fibers are neglected, the free fiber population behaves as a Newtonian suspension of an effective particle volume fraction $\varphi\Phi_2$ with a relative shear viscosity given by the following formula[b] [36]:

[b] Equation (7) is obtained from Eq. (2.26) of the original paper [36] by replacing the constant k by $3\pi(d+h_H)/h_H$ and neglecting the last adhesion term in the right-hand side of this equation.

$$\eta_f^r = \frac{\eta_f}{\eta_0} = 1 + 2(\varphi\Phi_2) + \frac{2}{3}c(\varphi\Phi_2)\frac{r\ln^{1/2}(r)f^{II}}{\ln(2r)} + \frac{8}{\pi}c(\varphi\Phi_2)^2\left(1+\frac{d}{h_H}\right)r\ln^{1/2}(r) \qquad (7)$$

where $f^{II} = (1+0.64\varepsilon)/(1-1.5\varepsilon)$ is the form factor; $\varepsilon = 1/\ln(2r)$ and $c \approx 0.254$. The last two terms of Eq. (7) stand respectively for hydrodynamic interactions between the fibers and the solvent and for short-range lubrication forces between contacting fibers.

Notice that the relative viscosity of the whole disaggregated suspension at high shear plateau is defined by Eq. (7) where the fraction of free fibers Φ_2 is set to unity: $\Phi_2=1$.

II-C. Mechanical equilibrium of the aggregates and suspension viscosity

According to the assumption (3) [Sec. II-A], the rigid impermeable clusters are dispersed in a Newtonian fluid formed by the population of free fibers suspended in the liquid solvent. The volume fraction of the aggregates is $\varphi_a = \varphi\Phi_1/\varphi_i$, and the relative viscosity of the suspension of the aggregates dispersed in the continuous medium of viscosity η_f is estimated by the Krieger-Daugherty relationship [3]:

$$\eta_a^{\,r} = \frac{\eta_a}{\eta_f} = \left[1-\frac{\varphi_a}{\varphi_{m,a}}\right]^{-[\eta]\varphi_{m,a}} = \left[1-\frac{\varphi\Phi_1}{\varphi_{m,a}\varphi_i}\right]^{-[\eta]\varphi_{m,a}} \qquad (8)$$

where $[\eta]$ is the intrinsic viscosity of a dilute suspension of aggregates, $\varphi_{m,a}$ is their maximum packing fraction. The value $[\eta] = 5/2$ allows recovering a dilute hard sphere suspension limit for aggregates at high shear rates, while the maximum packing fraction is forced to unity, $\varphi_{m,a} \sim 1$, that is appropriate for a continuous fiber network occupying all the suspension volume, which is expected in the quiescent suspension.

The relative viscosity $\eta_a^{\,r}$ depends on the two unknown parameters Φ_1 and φ_i. The fraction Φ_1 of aggregated fibers will be estimated in Sec. II-D. The internal volume fraction φ_i of aggregates is determined in this section.

According to the assumption (7.3) [Sec. II-A], all the aggregates are supposed to have the same internal volume fraction corresponding to the limit of their mechanical stability under shearing forces. The adhesive forces between fibers are capable to preserve the aggregates from destruction until they are dominant over the shearing forces.

The aggregate break-up can follow two different scenarios: (a) erosion of individual fibers from the aggregate surface, or (b) aggregate rupture and splitting into parts, both mechanisms being observed in flexible cellulose suspensions [60]. The dominant break-up mechanism has to be found for our particular case of rigid fiber suspensions. To this purpose, it is convenient to compare the shear stresses corresponding to aggregate destruction by both

mechanisms. Estimation shows that the rupture stress, $\sigma_r = 32\varphi_i^2 r F_A/(5\pi d^2)$ appears to be lower than the erosion stress, $\sigma_e = 32\varphi_i r F_A/(5\pi d^2)$ (cf. Sec. B of Supplemental Materials) [42], or, in other words, the fracture occurs at lower stresses and therefore is expected to be a dominant mechanism of the aggregate destruction.

We suppose therefore that the aggregates are broken in equal parts by shearing forces. The hydrodynamic force acting on a half of a broken aggregate is maximal along the extension axis. Therefore, the fracture is assumed to happen at the aggregate middle plane perpendicular to the extension axis of the shear flow, making an angle π/4 with the flow direction [Fig. 1b] Note that appearance of the voids inside the flocs under shearing forces has been reported by Björkmann [61] and Karppinen *et al*. [62] for micro-fibrillated cellulose suspensions. These voids were extended along the largest compression axis (therefore perpendicular to the extension axis) and led to partial breakup of the fiber network.

The aggregate fracture corresponds to a break-up of the adhesive contacts within the fracture region. It is expected to occur when the hydrodynamic force, F_h, acting on a half of the aggregate surface overcomes the aggregate cohesive strength, F_c, defined by the sum of all adhesive forces in the fracture region. Both F_h and F_c represent the projection of the forces onto the extension axis along which the aggregate is torn.

Since the concentration φ_a of aggregates in the suspension is high enough, the hydrodynamic force acting on aggregates will be affected by multi-body hydrodynamic interactions with neighboring aggregates. These interactions can be accounted for by an effective medium approach considering that the aggregates are immersed into a fluid whose viscosity is equal to the viscosity η of the whole suspension rather than the viscosity η_f of the suspending medium. Such an approach has been successfully used by Snabre and Mills [41] for aggregated suspensions of spherical particles. At this condition, the hydrodynamic force acting on a half of the aggregate along the extension axis is given by the following expression [63]:

$$F_h = \frac{5\pi}{8}\eta\dot{\gamma}D^2 = \frac{5\pi}{8}\sigma D^2 \tag{9}$$

where D is the aggregate diameter and σ is the applied shear stress.

Similarly to lubrication forces between free fibers, the normal adhesive force F_n between aggregated fibers is expected to be proportional to the inter-fiber contact area, thus inversely proportional to the sine of the angle δ between fibers ($\sin\delta = \left|\mathbf{p}^\alpha \times \mathbf{p}^\beta\right|$, cf. Fig.1c) [11]:

$$F_n = \frac{F}{\left|\mathbf{p}^\alpha \times \mathbf{p}^\beta\right|} \tag{10}$$

where F is the value of the normal adhesive force corresponding to the angle $\delta=\pi/2$ between two fibers. In the particular case of van der Waals interaction, equation (10) holds at $r^{-1} \le \delta \le \pi/2$ and, at small separations $h_A << d$ between the fiber surfaces, the expression for F reads [64]:

$$F = \frac{A}{12}\frac{d}{h_A^{\,2}} \tag{11}$$

where A is the Hamaker constant.

The cohesive strength, F_c, of the aggregates is estimated in Appendix A for both normal and tangential rupture scenarios [assumption (4)] and for both isotropic and nearly aligned fiber orientation within the aggregates [assumption (7.1)]. These four cases are combined into a single expression for F_c:

$$F_c = -\frac{4\varphi_i^{\,2} F_A D^2 r}{\pi d^2} \tag{12}$$

where r and d are the fiber aspect ratio and diameter, respectively, $F_A = \xi F$ is an effective colloidal force, where the multiplier ξ is of the order of unity and varies in a narrow range $\min(1/2, \pi\mu/4) \le \xi \le \max(1, \mu)$ depending on the contact rupture scenario and the orientation state. The reasons for a weak variation of the cohesive strength with the rupture scenario and with the orientation distribution are explained in details in Appendix A. On the other hand, the characteristic value of the normal adhesive force, F, can be estimated using Eq. (11) if the separation h_A between aggregated fibers is known. In the present model, the value $F_A \sim F$ is taken as an adjustable parameter, which will allow us to estimate the separation h_A [Sec. IV-C, Appendix D].

At mechanical equilibrium, the sum of the hydrodynamic [Eq. (9)] and cohesive [Eq.(12)] forces is zero, and we arrive at the following expression for the desired quantity – the internal volume fraction of aggregates:

$$\frac{1}{\varphi_i^{\,2}} = \frac{32 F_A r}{5\pi^2 \sigma d^2} = \frac{32 N_A r}{5\pi^2}, \tag{13}$$

where we have made use of Eq. (2) for the aggregation parameter N_A.

The equation (13) gives a progressive increase of the internal volume fraction with an increase of the shear stress. This comes from the fact that the total number of contacts inside the fracture region (proportional to $\varphi_i^{\,2}$) should increase in order that the aggregate might support a higher applied stress. In such a way, the cohesive strength of the aggregate increases with the increasing stress; this ensures the balance of hydrodynamic and cohesive forces acting on the aggregate. At high shear stresses, the aggregation parameter vanishes, $N_A << 1$,

and the volume fraction becomes much larger than unity: $\varphi_i >> 1$. This indicates that the present model is only valid for moderate-to-high aggregation state, $N_A > 1$ ensuring physically correct values of the internal volume fraction $\varphi_i < 1$. To extend our model to high shear states, we add a term $1/\varphi_{m,i}^{\ 2}$ to the right-hand side of Eq. (13), allowing an upper limitation of the φ_i value by some maximum admissible internal volume fraction $\varphi_{m,i}$:

$$\frac{1}{\varphi_i^{\ 2}} = \frac{32 N_A r}{5\pi^2} + \frac{1}{\varphi_{m,i}^{\ 2}} \tag{14}$$

For definiteness, we put $\varphi_{m,i}$ equal to the upper limit concentration of the colloidal glass state: $\varphi_{m,i} = 5.4/r$. Notice that the aggregate diameter *D* disappears from Eq. (14) for φ_i. This has been expected thanks to non-fractal nature of the aggregate structure [assumption (7.2)].

Finally, substituting Eq. (14) for φ_i into Eq. (8), we get the following expression for the relative viscosity of the suspension of spherical aggregates dispersed in a free fiber suspension:

$$\eta_a^{\ r} = \left[1 - \frac{\varphi \Phi_1}{\varphi_{m,a}} \left(\frac{32 N_A r}{5\pi^2} + \frac{1}{\varphi_{m,i}^{\ 2}} \right)^{1/2} \right]^{-[\eta]\varphi_{m,a}} = \left[1 - \varphi \Phi_1 \left(\frac{32 F_A r}{5\pi^2 \sigma d^2} + \frac{1}{\varphi_{m,i}^{\ 2}} \right)^{1/2} \right]^{-5/2} \tag{15}$$

The equation (15) allows one to find the relative viscosity of the aggregate population as function of the aggregation parameter N_A (or, alternatively, the applied stress σ) and of the particle volume fraction φ. The viscosity of the whole suspension is found as the product of the relative viscosity $\eta_a^{\ r}$ of the aggregate suspension and the viscosity η_f of its suspending medium – the free fiber population:

$$\eta = \eta_f \eta_a^{\ r} = \eta_0 \eta_f^{\ r} \eta_a^{\ r} \tag{16}$$

where η_0 is the Newtonian solvent viscosity, $\eta_f^{\ r}$ is given by Eq. (7) and $\eta_a^{\ r}$ - by Eq. (15).

It is important to notice that the viscosities $\eta_f^{\ r}$ and $\eta_a^{\ r}$ of both fiber populations are affected by the average number *Z* of contacts per fiber. This effect is considered in details in Appendix B.

To close the problem, we need to define the fractions Φ_1 and Φ_2 of fibers belonging to both populations, since these quantities appear in the suspension viscosity.

II-D. Kinetic equation for the fractions Φ_1 and Φ_2

Kinetics of aggregation and of destruction of the aggregates is a complicated multiscale process. The aggregation is usually governed by the collisions between the aggregates of different sizes and is satisfactorily described by Smoluchowsky equation [65] allowing estimation of the aggregate size distribution. If the aggregation of spherical particles is well documented, the aggregation of fibers is studied only scarcely [66, 67] likely because of complexities related to orientational ordering and intricate cluster geometry. Development of a rigorous multiscale approach of the aggregation kinetics is out of scope of the present study.

Let n_1 and n_2 number density of particles belonging to populations of aggregated and free fibers, respectively, while n is the number density of all particles in the suspension. The particle conservation implies $n = n_1 + n_2$. The kinetic equations of both populations are written in the most general form, as follows:

$$\frac{dn_1}{dt} = q_c - q_d \tag{17a}$$

$$\frac{dn_2}{dt} = -q_c + q_d \tag{17b}$$

where t is the time; q_c and q_d are, respectively, the aggregate construction and the aggregate destruction rates per unit volume of the suspension. The sum of both kinetic equations gives $dn/dt = 0$ that verifies the particle conservation condition.

The aggregate construction is supposed to be governed by the fiber collision frequency, whose volume density has been estimated theoretically [8] and then confirmed by simulations [68]:

$$q_c \sim n_2^{\,2}\dot{\gamma} l^3 \frac{\ln r}{r^2} \sim n_2^{\,2} V_f \dot{\gamma} \ln r \tag{18}$$

where V_f, l and r are, respectively, the fiber volume, length and aspect ratio. The aggregation rate is then given by the product of the collision rate to the probability α_0 that the collision sticks the fibers together, also called the orthokinetic capture efficiency [69] and takes the form:

$$q_c = k_1 \alpha_0 n_2^{\,2} V_f \dot{\gamma} \ln r \tag{19}$$

where k_1 is a dimensionless constant accounting for geometrical details of the fiber-fiber collisions.

According to the fracture scenario introduced in Sec. II-C, the aggregate destruction is supposed to be governed by the fracturing of unstable aggregates having an internal volume fraction φ_i lower than that given by Eq. (14) and thus having an insufficient cohesive strength to resist to the shearing forces. The broken halves are expected to have nearly the same internal volume fraction as the original aggregate; they are therefore unstable and subject to a further fracturing. Thus, the first break-up could initiate a continuous fracturing-break-up process until the aggregates are fully disintegrated into separate fibers. In such a scenario, the destruction rate is given by:

$$q_d = n_a J \sim n_a n_i V_a \dot{\gamma}\,, \tag{20}$$

where n_a is the number density of the aggregates in the suspension; J is the number of fibers per unit time moving apart from the destroyed aggregate under the action of the shear flow, n_i is the number density of the fibers in the aggregates, and V_a is the aggregate volume. The product $n_a n_i$ appearing in the last equation is related to the number density n_1 of the aggregated fibers by the following expressions: $n_a n_i = n_1 / V_a$. The destruction rate is corrected by the term $1-\varphi/\varphi_i$ to ensure zero rate when the fiber concentration in the suspension, φ, approaches the internal volume fraction φ_i of aggregates – the yield point at which a continuous fiber network is expected to occur. In this way, topological interactions between fibers are implicitly taken into account. The final expression for the volume density of the destruction rate reads:

$$q_d = k_2 n_1 \dot{\gamma}\left(1-\frac{\varphi}{\varphi_i}\right) \tag{21}$$

with k_2 - a dimensionless constant, accounting for microscopic details of the aggregate destruction. Combining together Eqs. (17a), (19) and (21), the kinetic equation for n_1 is written in its final form:

$$\frac{dn_1}{dt} = k_1 \alpha_0 V_f \dot{\gamma} \ln(r) n_2^{\,2} - k_2 \dot{\gamma} n_1 \left(1-\frac{\varphi}{\varphi_i}\right) \tag{22}$$

The number densities n_1 and n_2 are related to the fractions Φ_1 and Φ_2 of the aggregated and free fibers by the following expressions: $n_1 = \Phi_1 \varphi / V_f$ and $n_2 = \Phi_2 \varphi / V_f$. Replacing these formulas in Eq. (22) and taking into account the particle conservation [Eq.(1)], we arrive at the following equation with respect to Φ_1:

$$\frac{d\Phi_1}{dt} = k_1 \alpha_0 \dot{\gamma} \ln(r) \varphi (1-\Phi_1)^2 - k_2 \dot{\gamma}\, \Phi_1 \left(1-\frac{\varphi}{\varphi_i}\right) \tag{23}$$

This equation admits the following steady state solution (at $d\Phi_1 / dt = 0$):

$$\Phi_1 = 1 + \lambda - \left[\lambda(\lambda+2)\right]^{1/2} \tag{24a}$$

$$\lambda = \kappa \frac{1-\varphi/\varphi_i}{2\alpha_0 \varphi \ln r} \tag{24b}$$

where $\kappa = k_2 / k_1$ is a dimensionless constant taken as an adjustable parameter of the present model and φ_i is given by Eq. (14) as function of the applied stress σ. The fraction Φ_2 of the free fibers is obtained from Eqs. (1) and (24a):

$$\Phi_2 = 1 - \Phi_1 = \left[\lambda(\lambda+2)\right]^{1/2} - \lambda \tag{25}$$

The last unknown parameter intervening into the expressions (24a) and (25) for Φ_1 and Φ_2 is the sticking probability α_0 given by the following expression estimated in Appendix C:

$$\alpha_0 \sim e^{-(\ln(2r) N_A)^{-1}} \tag{26}$$

where the aggregation parameter N_A is related to the applied shear stress σ by Eq. (2).

In summary, the suspension shear viscosity η is calculated by Eqs. (7), (15), (16), in which the fiber fractions Φ_1 and Φ_2 are replaced by Eqs. (24) and (25), respectively. The three adjustable parameters of the model are the gap h_H between free fibers, the effective adhesive force F_A, and the parameter κ appearing in the expression [Eq. (24)] for the fraction Φ_1 of aggregated fibers.

III. Experiments

In this work two kinds of fiber suspensions were investigated: polyamide fiber (PA) and carbon nanotube (CNT) suspensions. The characterization and experimental measuring protocols for PA suspensions will be presented in Sec. III-A and III-B, while the CNT suspensions will be briefly characterized in Sec. III-C.

III-A. Polyamide fiber suspensions

The PA fibers (provided by "La société nouvelle le flocage", France) of the length l=0.5 mm and of two different diameters, d=15.2±0.5 μm and 27.8±0.5 μm, corresponding to aspect ratios of r=33±1 and 18±0.5, were used. The fibers were monodisperse and their size was confirmed by optical microscopy measurements. The fiber density was measured precisely by a pycnometer method. Table I summarizes the size, the density and the effective stiffness (Eq. (S-16) in Supplemental Materials) [42] of both types of fibers.

The fiber surface roughness has been measured using an atomic force microscope (AFM). We obtained the values h_R=5±2 nm and h_R=14±4 nm of the arithmetic average roughness (R_a) for the fibers of the aspect ratios, r=18 and r=33, respectively.

Table I. Characterization of PA fibers and CNT

Material	Length l [μm]	Diameter d [μm]	Aspect ratio r	Density ρ_f [g/cm^3]	Effective dimensionless stiffness, S_{eff}***
PA	500	15.2±0.5	33±1	1.340±0.001	$4 - 4\cdot10^4$
PA	500	27.8±0.5	18±0.5	1.090±0.001	$30 - 3\cdot10^5$
CNT	0.1-2.2 (0.5)*	0.007-0.025 (0.014)*	4-314 (36)**	≈2.0	$0.4 - 4\cdot10^3$

* The values in brackets correspond to the peak of the size distribution of CNT reported by Khalkhal *et al*. [37];
** The value in brackets correspond to the ratio of the peak value of the CNT length to the peak value of its diameter
*** Estimations are provided in Sec. C of Supplemental Materials [42]

Table II. Characterization of the suspending liquid of the fiber suspensions

Fibers	Composition	Density ρ_0 [g/cm^3]	Viscosity η_0 [Pa·s]	Ionic strength I [mol/L]*
PA, r=33	Ucon oil (30%vol)/ water (70%vol) / $ZnBr_2$ (404 g/L)	1.340±0.001	0.310±0.010 at 20°C	4.5
PA, r=18	Ucon oil (40%vol)/ water (60%vol) / NaBr (92.6 g/L)	1.090±0.001	0.364±0.010 at 20°C	0.9
CNT, r=36	Epoxy Epson 828 (HEXION Specialty Chemicals Inc.)	1.16	12.33 at 25°C	N/A

* Estimations are provided in Sec. C of Supplemental Materials [42]

The PA fibers were dispersed in a mixture of UCON oil 75H90000 (Dow Chemical, France; density ρ_{oil}=1.09 g/cm^3, viscosity η_{oil}=30 Pa·s at 25°C) in distilled water at different volume fractions φ ranging from 1 to 17% depending on the fiber aspect ratio. This mixture has been chosen as a model system, ensuring the neutral buoyancy and having a relatively low viscosity that allows attaining a relatively high ratio of colloidal-to-hydrodynamic forces required for studies of the shear thinning behavior. Furthermore, UCON oil shows a good solubility in water without phase separation, and the mixture exhibits a perfectly Newtonian

response in the considered range of the shear rates, $10^{-2} < \dot{\gamma} < 10^{2}$ s^{-1}. An appropriate amount of zinc bromide ($ZnBr_2$) or sodium bromide (NaBr) salt [Sigma-Aldrich, France] was added into the mixture in order to adjust the density of the suspending liquid to that of the fibers. The composition of the suspending liquid for both fiber sizes is summarized in Table II along with its physical properties.

The fiber sedimentation time scale, the fiber effective stiffness Péclet and Reynolds numbers, inertial pressure, Debye screening length and Hamaker constant of PA/UCON-water system are estimated in Sec. C of Supplemental Materials [42]. These estimations allow us to draw the following conclusions on PA suspensions:

(a) the assumption (1) on rigid non-Brownian (Péclet number is $Pe \approx 3\times10^{7}$) and neutrally buoyant fibers is confirmed;

(b) the assumption (2) on laminar flow on the flow scale (Reynolds number $Re_{flow} \approx 360$) and particle scale ($Re_p \approx 4\times10^{-3}$) is validated;

(c) the electrostatic interactions are completely screened by a relatively large amount of brome salts added to the suspending fluid resulting in Debye length κ_e^{-1}<1 nm; PA suspensions are therefore fitted into the frames of our model developed for attractive interactions [assumption (3)].

The same conclusions hold for CNT suspensions, as follows from appropriate characterizations and estimations done in the work of Khalkhal *et al*. [37].

The quiescent PA fiber suspensions were visualized after shearing using an inverted optical microscope Nikon Dashpot. The micrographs shown in Fig. 2 confirm some spatial heterogeneity at relatively low suspension concentration.

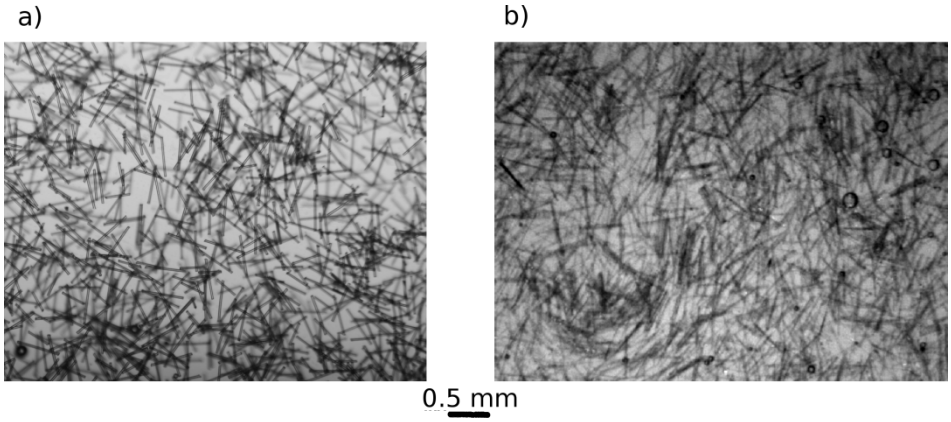

Fig. 2. Optical microscopy images for quiescent PA fiber suspensions. The figure (a) corresponds to particle aspect ratio r=18 and φ=0.03; the figure (b) – to r=33 and φ=0.05

Existence and behavior of concentration heterogeneities can be better analyzed via observation of the suspension behavior under shear. The video available in Supplemental

Materials [70] (best viewed in Google Chrome or Safari browsers) shows the shearing of the suspension of fiber volume fraction φ=0.05 and aspect ratio r=18 at a shear rate 0.3 s^{-1} and at the gap between moving plates fixed to three fiber lengths. The experiment starts with a short and intense pre-shear at 50 s^{-1} applied before the main shearing at 0.3 s^{-1} in order to be closer to the experimental protocol of the rheometric measurements [Sec. III-B]. The following information can be drawn from this observation: (a) the existence of denser domains separated by free fibers is confirmed; (b) the fibers belonging to these domains seem to exhibit a cooperative motion and some misalignment relatively to each other; (c) it was impossible to measure the spatial correlation of fiber velocities but we estimated the spatial correlation of the particle concentration applying a Fourier transform to the image intensity and assigning the lowest harmonic to the correlation length; this length was about one-to-two fiber lengths, D~(1–2)l, and was taken as a rough estimate of the aggregate size; notice that density and velocity correlation lengths could be different, thus an exhaustive experimental study is required for a precise determination of the aggregate size distribution; (d) some domains have an isotropic shape, other ones – an extended shape aligned with the main flow, however the Fourier analysis appears to be very rough to indicate precise values of the aggregate aspect ratio; it is estimated to lie in the range $1<r_a<3$; (e) some rearrangement of fibers inside the denser domains is observed but it is difficult to follow kinetics of their formation and disintegration because of their small travel distance limited by the narrow observation window. Even though more accurate image processing would be necessary to well characterize the aggregate morphology, we believe that these observations are in agreement with our basic assumptions (3.1)-(3.4) concerning particle aggregation, as we defined it in Sec. II-A.

III-B. Experimental procedure on polyamide fiber suspensions

The viscosity measurements are carried out with a controlled-stress rheometer (Thermo Mars II) in rotating parallel plate geometry. The suspension is introduced into a pool and sheared by a rotating top disk, as shown schematically in Fig. 3. The suspension level in the pool is adjusted to the upper surface of the rotating plate. This allows minimization of capillary pressure effects and shear rate oscillations at low shear rates. The pool is covered by a Plexiglas lid in order to minimize evaporation of the suspending liquid. The temperature of the lower plate (bottom of the pool) is kept constant and equal to 20°C by a standard Peltier element, while the experimental room is air conditioned at 22°C. The measuring system had the following dimensions: the rotating plate and the pool radii were R_{plate}=30 mm and R_{pool}=44 mm, respectively. The gap between the rotating plate and the bottom of the pool was varied in the range b=2-10 mm. This geometry was chosen in order to decrease possible effects of the fiber or aggregate confinement in the measuring gap. However, due to shearing of the suspension in the pool outside the gap, this geometry gives overestimated values of the viscosity and the appropriate correction is described in Sec. C of Supplemental Materials [42].

To check the confinement effect, we have measured the suspension viscosity in the pool geometry at different gaps b, ranging from 1 to 6 mm. The measurements show that the

suspension viscosity becomes independent of the gap at b>4 mm. We expect therefore that the confinement effects are negligible when the gap is set to b=5 mm for all the measurements reported in the present paper. This is also consistent with the scale separation, $D << b$ assumed in our model [assumption (8)] and approximately verified in visualization experiments [Sec. III-A], where $D \sim (1-2)l = 0.5-1$ mm is the aggregate length scale.

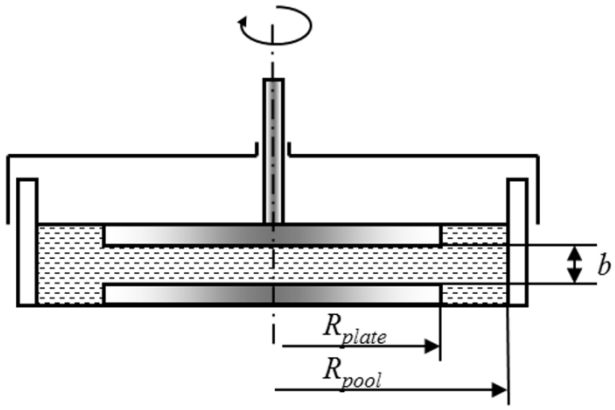

Fig. 3. Sketch of the experimental pool geometry

The measurements are performed in a controlled-stress mode using the following protocol. First, the suspension is pre-sheared for 3 min at $\dot{\gamma} = 10^2$ s^{-1}. Then, the suspension is left at rest for 3 min. Then, the constant shear stress of the lowest value (corresponding approximately to $\dot{\gamma} = 10^{-2}$ s^{-1}) is applied for a time ranging between 2 and 5 h, long enough to ensure that the steady state has been reached. The shear rate and the suspension viscosity are measured as function of time. At the end of this period, the suspension is left un-sheared for 3 min, and sheared again for 3 min at $\dot{\gamma} = 10^2$ s^{-1}, left un-sheared once more for 3 min, and a new value of the constant shear stress is applied for a time sufficient for reaching the steady-state. For adequate comparison with the theory, the Moony correction is applied to the shear stress and the shear viscosity, as explained in details in Sec. C of Supplemental Materials [42]. This procedure with a pre-shear stage is repeated for all the values of the applied shear stress (increasing at each new step) until its highest value corresponding to $\dot{\gamma} = 10^2$ s^{-1}. In some cases, the measurements have also been continued by a decreasing shear stress ramp. And, even though the full measurement lasts several hours, we did not observe distinguishable flow curve hysteresis and the low-shear steady-state viscosity was found to be the same at the beginning and the end of the test. This proves the absence of sedimentation and evaporation of the suspending liquid, in agreement with the estimation by Eq. (S-14) in Supplemental Materials [42], as well as the absence of aging effects. Furthermore, shear-induced particle migration, either within the gap or from the inside to outside of the gap, appears not to play any role, in agreement with the assumption (8) and with the experimental data on suspensions of spherical particles in parallel plate geometry [71-73].

It is important to note that our measuring protocol with high shear rate pre-shearing ensured the similar initial conditions for each value of the applied shear stress. This allowed us to exclude the effects of the shear history on the suspension rheology.

III-C. Carbon nanotube suspensions

The CNT suspensions have been characterized in details in the work of Khalkhal *et al*. [37]. Some parameters of the multiwall CNT particles are summarized in Table I. The particles showed a rather broad distribution of their length and diameter, with the values l=0.5 μm and d=14 nm corresponding to the peak of the size distribution curves. These values result in an effective aspect ratio r=36 and were used for the comparison between experiments and our model.

The multiwall CNTs were dispersed in a Newtonian epoxy resin Epson 828 (HEXION Specialty Chemicals Inc.) having a viscosity η_0=12.3 Pa.s at 25°C at different volume fractions φ ranging from 0.59 to 2.36%. The estimations using Eqs. (S-14)-(S-16) in Supplemental Materials [42] allow one to neglect the CNT settling during experiments and consider them as rigid and non-Brownian within the experimental range of applied shear rates, even though the electron microscopy reveals some bending of fibers likely because of some local defects. The Hamaker constant for CNT/epoxy system was evaluated to be A~10^{-20} J (cf. Sec. C of Supplemental Materials) [42]. Unfortunately, there is no more precise information about colloidal interactions between the CNT and their surface roughness.

A torsional cone-plate flow was realized using an Anton Paar Physica MCR 501 rheometer in a controlled-rate mode with a rotating cone having a diameter of 50 mm and an apex angle of 2°. The shear rate is homogeneous in this geometry, and any rheological correction is not required. The flow respected the non-inertia limit according to the estimations of the Reynolds numbers and of the inertial pressure (cf. Eqs. (S-19) and (S-20) in Supplemental Materials) [42]. The experimental protocol is described in details in the work of Natale *et al*. [34].

IV. Results and discussion

IV-A. Transient response

Experimental time dependency of the viscosity of PA fiber suspension during all the measurement corresponding to the increasing stress ramp including pre-shearing stages between each applied stress is shown in Fig. 4a for the particle volume fraction φ=0.09 and aspect ratio r=18. The time dependency of the imposed shear stress is also shown on this figure. As is seen from this figure, the total duration of the measurement is about 10.5h. The duration of the longest measurement step between intense pre-shearing steps (that are expected to re-suspend the particles) is 2h and is smaller than the typical settling time of 7h, estimated by Eq. (S-14) in Supplemental Materials [42].

A detailed view of the second and the third stress steps (σ=0.2 Pa and 0.3 Pa) is presented in Fig. 4b for the same suspension. This figure deserves some comments. Firstly, the viscosity signal for σ=0.2 Pa is quite noisy probably because such a small imposed stress generates an extremely low shear rate of about $2 \cdot 10^{-3}$ s^{-1} being near the detection limit of the rheometer. Another possible reason could come from an unstable and inhomogeneous flow of highly aggregated suspension at very low shear rate near the yield point. The viscosity signal becomes rather smooth and regular starting from the imposed stress equal to 0.3 Pa.

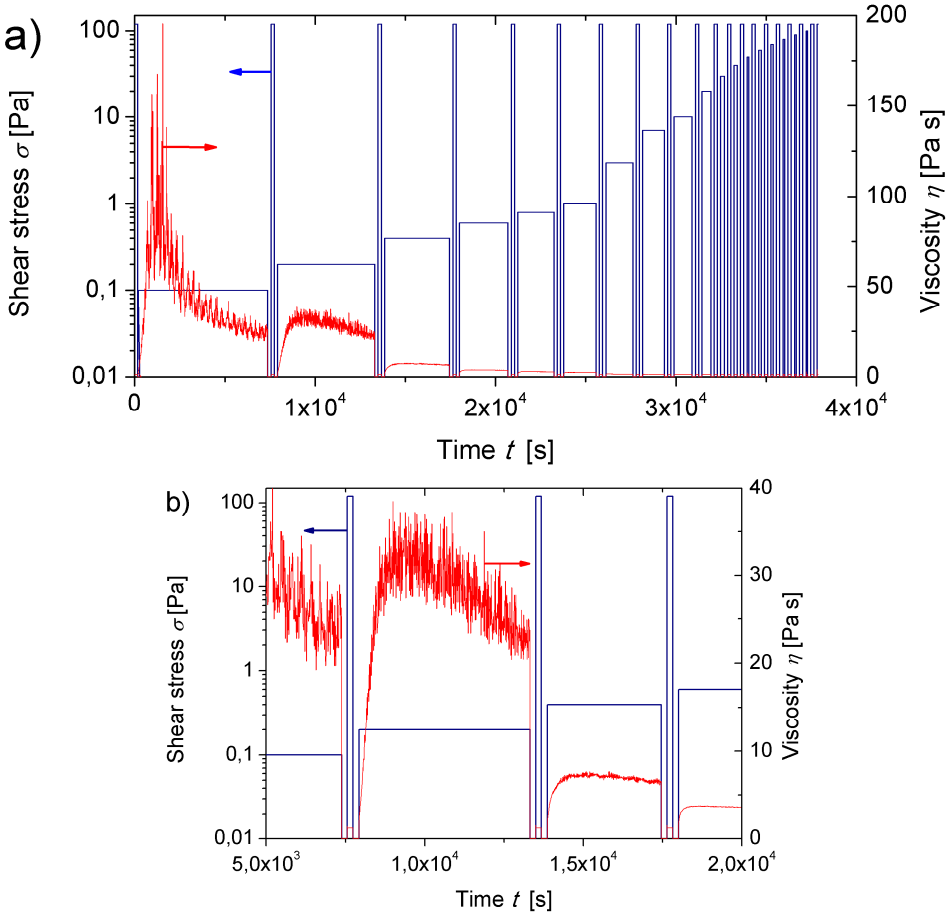

Fig. 4. Transient rheological response of a PA fiber suspension with a particle aspect ratio r=18 and a particle volume fraction φ=0.09. The figure (a) corresponds to the whole duration of the experiment; the figure (b) is a detailed view of the second and third stress steps at imposed shear stress equal to σ=0.2 Pa and 0.3 Pa. On both graphs, the blue line corresponds to the imposed stress $\sigma(t)$; the red curve – to the viscosity $\eta(t)$. Raw values of the viscosity are presented in figures (a) and (b) without performing the correction due to the pool geometry.

Secondly, very large times are required to achieve the steady state viscosity at low shear rates $\dot{\gamma} \sim 10^{-2}$ s^{-1}. This can be easily understood in terms of slow orientation dynamics of fibers in the shear flow. The Jeffery period of the rotation of high aspect ratio fibers is given by [3]: $T_{rot} \approx 2\pi r / \dot{\gamma}$ that gives about 3h for r=18 and $\dot{\gamma} = 10^{-2}$ s^{-1}. Even though the fibers are pre-oriented by intense pre-shearing at the beginning of each measurement, they spend almost half of the Jeffery period being nearly aligned with the flow and trying to readjust their mean

orientation to the new steady state value. Another possible reason for a slow dynamics is the kinetics of aggregation. The aggregation governed by pair collisions between fibers has a time scale of $T_{agr} \sim \dot{\gamma}^{-1}$. A more precise estimation based on the solution of the kinetic equation (23) gives the value of about 0.5h for the time required for the fraction, Φ_1, of aggregated fibers to reach 95% of its steady state value at $\dot{\gamma} = 10^{-2}$ s^{-1}, r=18 and φ=0.17 [we set $k_1 = k_2 = \alpha_0 \sim 1$ in Eq.(23)]. Thus, taking into account uncertainties in kinetic coefficients k_1 and k_2, kinetics of aggregation and orientation could have comparable time scales, both governing the long-time transient response of the suspension.

IV-B. Steady-state: high shear viscosity

The steady-state values of the shear rate and of the suspension viscosity at a given shear stress σ were calculated by the time averaging of the experimental $\dot{\gamma}(t)$ and $\eta(t)$ dependencies [Fig. 4] over the last quarter of the corresponding time interval. Before the study of the suspension shear thinning, it is important to inspect the high shear rate response when all the aggregates are expected to be destroyed and the suspension should behave as a Newtonian fiber suspension in absence of non-hydrodynamic interactions. The theoretical and experimental dependencies of the high shear relative viscosity $\eta^r = \eta / \eta_0$ on the particle volume fraction φ is presented in Fig. 5a for PA fibers of both aspect ratios r=18 and 33.

The experimental values of η^r (symbols in Fig. 5a) were taken at the highest shear rate $\dot{\gamma} \approx 10^2$ s^{-1}, while the theoretical values (solid lines) where calculated by Eq. (7), in which the fraction of the free fibers was set to one: $\Phi_2 = 1$. As is seen from this figure, both experimental and theoretical concentration dependencies are stronger than linear indicating the presence of hydrodynamic interactions between fibers. The pair-wise lubrication interactions between free fibers have been taken into account in our model producing a term quadratic in particle volume fraction [last term in Eq. (7)]. Recall that the theoretical expression (7) contains one adjustable parameter – the gap h_H between the free fibers. A satisfactory fit of the experimental curves was ensured almost in the whole range of particle volume fractions φ except for the highest concentrations. The disagreement at high concentrations likely comes from the fact that pair-wise lubrication forces between free fibers are insufficient to describe the viscosity of highly concentrated suspensions. The following values of h_H were used to ensure the best fits: h_H=6 μm for the fibers of the aspect ratio r=33 and h_H=9 μm for r=18.

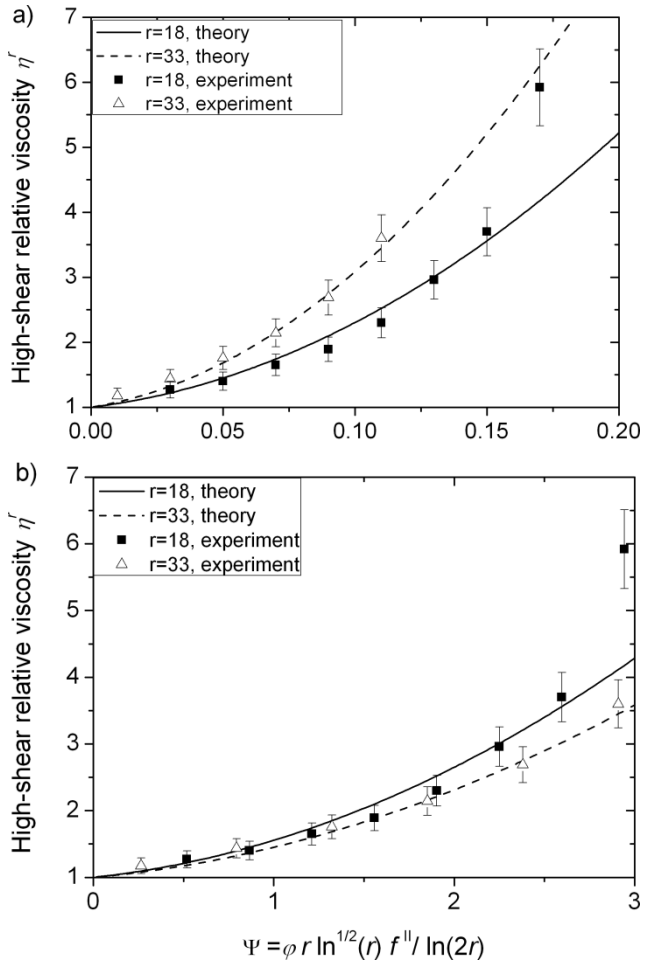

Fig.5. Experimental and theoretical dependencies of the relative high shear viscosity of the PA fiber suspensions on the particle volume fraction (a) and on the factor Ψ (b). Solid curves – theory [Eq. (7) with $\Phi_2 = 1$].

It is known that, in the low diffusion, $D_r r^3 / \dot{\gamma} << 1$, and high aspect ratio, $r >> 1$ limits, the relative viscosity of dilute-to-semi-dilute fiber suspensions is approximately proportional to the product φr of the particle concentration and the fiber aspect ratio [3, 58]. More precisely, according to Eq. (7), we expect that the relative viscosity η^r is proportional to the factor $\Psi = \varphi r \ln^{1/2}(r) f^{II} / \ln(2r)$ in the low concentration limit, $\varphi(1 + d / h_H) << 1$, when the lubrication forces between fibers give a negligible contribution to the suspension viscosity. In this case, the data for fibers of different aspect ratios are expected to fit onto a single master curve $\eta^r = f(\Psi)$. To check this point, we plot experimental and theoretical dependencies of the relative viscosity on the factor Ψ on Fig. 5b for both aspect ratios r=18 and 33. The experimental data for two aspect ratios collapse in a single curve in a relatively wide range of factors Ψ, namely $0<\Psi<2$, while the data diverge at $\Psi \approx 3$.

Notice that our aggregation model [Sec. II-C] allows recovering the high shear viscosity [Eq. (7)] due to the fact that, at high applied stresses, the sticking probability tends

to zero [Eq. (26)] such that the fraction of free fibers tends to unity, $\Phi_2 = 1$ [Eq. (25) with $\lambda \to \infty$ at $\alpha_0 = 0$].

IV-C. Steady-state: shear thinning behavior

Experimental and theoretical flow curves are shown on the left column of Fig. 6, while the shear rate dependency of the relative viscosity $\eta^r = \eta / \eta_0$ is shown on the right column of this figure, for PA fibers with aspect ratio r=18 [Fig. 6a], PA fibers with r=33 [Fig. 6b] and CNT dispersed in a Newtonian epoxy resin [Fig. 6c]. Theoretical $\sigma(\dot{\gamma})$ and $\eta(\dot{\gamma})$ dependencies are obtained in parametric form using $\dot{\gamma}(\sigma) = \sigma / \eta(\sigma)$. All the theoretical curves were fitted to experimental data using the set of the adjustable parameters (h_H, F_A, κ) summarized in Table IV of Appendix D. In what concerns the aggregate shape, analysis conducted in Sec. A of Supplemental Materials [42] shows that the aggregate aspect ratio r_a has only a minor influence on the suspension viscosity in the range $1 \le r_a \le 3$ corresponding to our experiments on PA suspensions. Therefore, all the calculations reported in the present paper correspond to the spherical aggregate shape.

All the theoretical and experimental flow curves shown on the left column in Fig. 6 share the following common features: (a) they show a shear-thinning behavior; (b) they are shifted upwards with increasing the particle concentration signifying an increase of the viscous dissipation. In double logarithmic scale, some experimental flow curves show a two step behavior with an intermediate quasi-plateau (Fig. 6b for r=33 and φ=0.07 and 0.09). Such a shape is reminiscent for shear banding and/or wall slip in complex fluids [74]. A similar flow curve shape has been observed in flocculated cellulose suspensions for which existence of shear banding and wall slip were confirmed by flow visualization and by measurements of the velocity profiles [11, 62, 75]. However, our preliminary observations under shear did not allow a clear justification for existence of shear banding, while the wall slip usually leads to a gap dependence of the suspension viscosity, which has not been detected for the gaps b>4 mm. Our model (solid lines) better reproduces the experimental flow curves at shear rates $\dot{\gamma} > 0.1$ s^{-1} and predicts a low shear plateau at $\dot{\gamma} < 0.1$ s^{-1} reminiscent for the yield stress [Sec. IV-D]. A discrepancy at low shear rates could come from the representation of the suspension structure by spherical aggregates instead of a continuous fiber network.

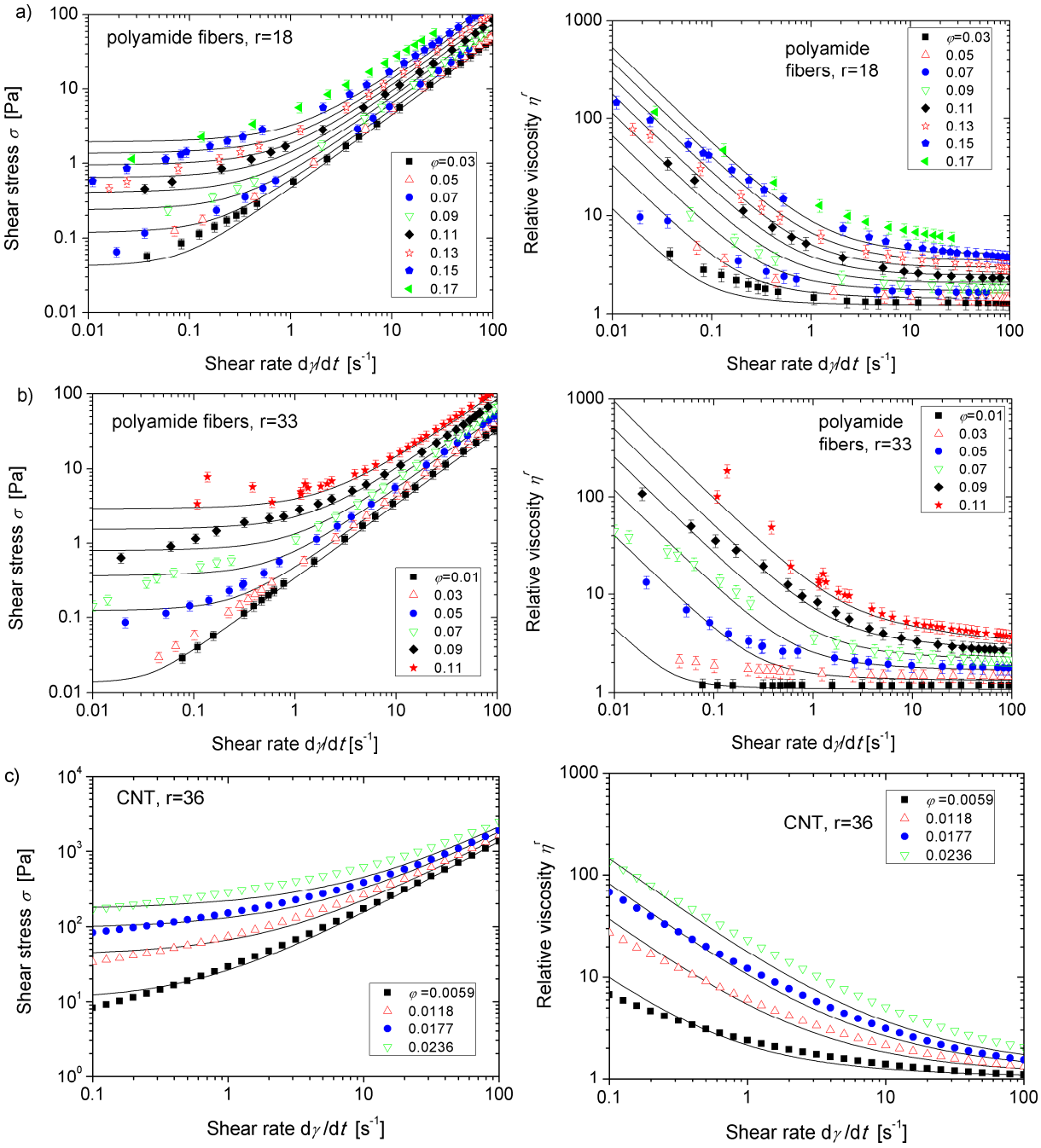

Fig. 6. Experimental and theoretical flow curves (left column) and viscosity versus shear rate dependences (right column) of different fiber suspensions at different particle volume fractions: PA microfibers with the particle aspect ratio equal to r=18 (a); PA microfibers with r=33 (b); and CNT with r=36 (c). Symbols correspond to experiments and solid lines – to the theory. The values of the adjustable parameters are summarized in Table IV in Appendix D.

The observed shear thinning behavior can be better analyzed with the help of the shear rate dependency of the relative viscosity [right column of Fig. 6]. Let us first analyze the curves corresponding to the PA fiber suspensions and then compare them to those corresponding to the CNT suspensions. Qualitatively, for PA fibers, both the theory (solid curves) and experiments (symbols) reveal a rather strong shear thinning with an increase of

the viscosity of more than one order of magnitude (compared to the high shear rate viscosity value) for the highest fiber concentrations. The high shear plateaus are well distinguished at relatively low particle volume fractions (φ<0.07 at r=18 and φ<0.05 at r=33). They are shifted to higher shear rate values when the particle volume fraction increases and disappear at the highest concentrations (φ>0.15 at r=18 and φ=0.11 at r=33). Such a shift is accompanied by a significant increase of the degree of shear thinning when the particle volume fraction becomes larger. These both concentration effects could be explained by an increasing role of the adhesive interactions between fibers when the particle volume fraction increases. Such concentration behavior is analyzed in details in Appendix E.

In what concerns the CNT suspensions [right graph on Fig. 6c], both theory and experiments also reveal a strong shear thinning with low shear viscosity at $\dot{\gamma} = 10^{-2}$ s^{-1} being two-to-three orders of magnitude higher than the high-shear viscosity at $\dot{\gamma} = 10^{2}$ s^{-1}. Estimation of the colloidal forces could clarify the reason behind a stronger shear thinning in CNT suspensions. By fitting the rheological curves to the experimental data, we obtain the value of the effective adhesive force F_A for PA fibers three orders of magnitude larger than for CNT [see Table IV, Appendix D], that is something expected because of the size difference between these two types of fibers. However, it is not the value F_A that directly affects the suspension viscosity but rather the ratio of colloidal to hydrodynamic forces N_A, or more precisely, the dimensionless factor $N_A r = F_A r/(\sigma d^2)$, as inferred from Eq. (15). At the same applied stress, σ, and nearly the same aspect ratio (r=33 for PA fibers and r=36 for CNT), the factor $N_A r$ for CNT is about 2×10^3 times higher than for PA fibers. At the same shear rate, say $\dot{\gamma} = 1$ s^{-1}, and nearly the same volume fraction (φ=0.01 for PA and 0.0118 for CNT), this difference reduces to 10 times because of much higher viscosity of the suspending liquid of CNT. Both estimations indicate a more pronounced role of colloidal interactions between nanoscale CNT compared to micron-sized PA fibers. As a consequence, the CNT aggregates better resist to the shearing forces and give a higher viscosity at low shear rates and thus a higher decrease in viscosity between the low-shear and high-shear regimes.

As is seen in Fig. 6, the best agreement between the theory and experiments is obtained at intermediate particle concentrations for both PA fiber suspensions [Figs. 6a, 6b] and CNT suspensions [Fig. 6c]. Some mismatch at the lowest concentrations likely comes from a non-spherical shape of the aggregates caused by collisions between the fibers mostly aligned with the flow at low particle volume fractions. The discrepancy at the highest concentrations (especially pronounced for PA fibers at r=18, Fig. 6a) can be related to different factors, such as (a) incorrect estimation of the high-shear viscosity under approximation of pair-wise interactions between fibers belonging to the free fiber population; (b) a more complex kinetics of aggregation/destruction rather than that considered in Sec. II-D. Despite of these disagreements, our model captures relatively well, both qualitatively and quantitatively, the shear thinning behavior of both the CNT and the PA fiber suspensions.

From the theoretical point of view, the shear thinning behavior is related to variable aggregate volume fraction, $\varphi_a = \varphi\Phi_1 / \varphi_i$ [Eq. (8)], and is therefore a combination of the shear rate dependencies $\Phi_1(\dot{\gamma})$ and $\varphi_i(\dot{\gamma})$. For the better understanding of the shear thinning behavior, we inspect these two dependences on Fig. 7 for PA fibers at the particle volume fraction φ=0.11 and for two considered aspect ratios.

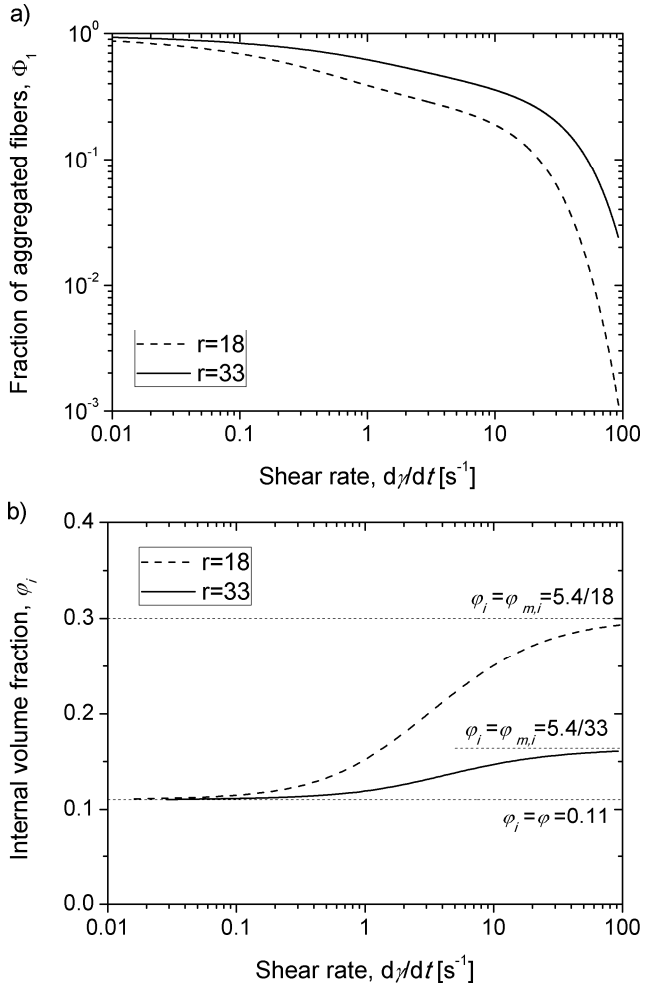

Fig. 7. Theoretical shear rate dependencis of the fraction Φ_1 of aggregated PA fibers (a) and of the internal aggregate volume fraction φ_i (b) for PA fibers at the particle volume fraction φ=0.11 and two aspect ratios r=18 and 33. The horizontal dotted lines on figure (b) indicate the lower (φ_i=φ) and the upper (φ_i=5.4/r) concentration limits for φ_i

The fraction Φ_1 of aggregated fibers exhibits a progressive decrease from unity at zero shear rate (fully aggregated state with a yield stress – see Sec. IV-D) to zero at high shear rates (fully unstructured suspension) – see Fig. 7a. We also note that the content of aggregates is higher for the fibers with a higher aspect ratio. The fraction Φ_2 of free fibers is related to the fraction Φ_1 of aggregated fibers by Eq. (1). Thus, Φ_2 follows an opposite tendency with increasing shear rate (not shown here for brevity): it increases progressively from zero at zero shear rate to unity at high shear rates. The internal aggregate volume fraction φ_i [Eq. (14)] also shows a monotonic increase with the shear rate [Fig. 7b] related to the fact that more

compact aggregates (with higher contact densities) better resist to increasing shear forces. At zero shear rate, φ_i tends to the particle volume fraction φ; this corresponds to a percolated fiber network with Φ_1=1. At high shear rates, φ_i approaches the upper concentration limit $\varphi_{m,i}$=5.4/r. The horizontal dotted lines in Fig. 7b correspond to the upper and the lower concentration limits of the internal volume fraction φ_i. Thus, the shear rate dependencies $\Phi_1(\dot{\gamma})$ and $\varphi_i(\dot{\gamma})$ amplify each other being in qualitative agreement with the shear thinning behavior observed on Fig. 6: progressive compactness and disappearance of aggregates with increasing shear rates leads to a gradual decrease of the suspension viscosity.

Finally, the obtained value of the adjustable parameter F_A allows *a posteriori* estimation of the inter-fiber separation h_A between the aggregated fibers, while another adjustable parameter directly gives the gap h_H between the free fibers. The details of this estimation are reported in Appendix D. Briefly, we get $h_H = (0.3-0.4)d \approx 6-9$ μm for free PA fibers and $h_A \sim (0.2-0.6)h_R \sim 3$ nm for aggregated fibers, with d≈15-28 μm being the fiber diameter and h_R~5-14 nm - surface roughness [Sec. III-A]. These values fit into the length scale ranges of hydrodynamic and colloidal interactions *a priori* supposed for free fibers and aggregated fibers respectively. Furthermore, the lubrication force between the free fibers (estimated by Eq. (4) with an appropriate value of h_H and $\left|\mathbf{p}^{\alpha}\times\mathbf{p}^{\beta}\right|$ set to unity] appears to be 8-10 orders of magnitude larger than the adhesive force F_A, in agreement with assumption (4) of Sec. II-A. Note that the value h_A~3 nm is somewhat lower than the fiber surface roughness h_R that likely indicates a close contact between fibers inside the aggregates with interlocking asperities. On the other hand, surface roughness is known to substantially increase the effective van der Waals attraction at close separations h_A between rough surfaces [76]. Therefore, the value of h_A~3 nm is likely underestimated. The same conclusions hold for CNT suspensions.

IV-D. Yield stress

Low shear plateau of the theoretical flow curves plotted in log-log scale and shown in Fig. 6 reveal some yield stress, which appears to be higher in CNT suspensions than in PA fiber suspensions. Experiments on PA fiber suspensions conducted in a stress-control mode also showed some small but measurable yield stresses at high enough particle volume fractions ($\varphi \geq 0.07$ at r=18 and $\varphi \geq 0.05$ at r=33). Experiments on CNT were carried out by Natale *et al*. [34] in shear rate-control mode, not allowing a direct measurement of the yield stress. However, potential yield stress for this suspension can be seen in flow curves plotted in a log-log scale – see Fig. 6c. It is worth noticing that, in contrast to the results of Natale *et al*. [34], other authors report a non-negligible yield stress in suspensions of CNT dispersed in the Newtonian epoxy solvent [77, 78]. They attribute the yield behavior to appearance of the network of nanotubes having a higher aspect ratio (80<r<1200) than those used by Natale *et al*. (r≈36) and being less stiff.

For a deeper understanding of the yielding behavior, let us find an explicit expression for the predicted yield stress. Similarly to the structural models of Snabre and Mills [41], Quemada and Berli [10], the yield stress arises in our model when the effective aggregate concentration $\varphi_a = \varphi\Phi_1/\varphi_i$ approaches the value $\varphi_{m,a}$ of the maximum packing fraction of aggregates and the fraction of aggregated fibers Φ_1 approaches to unity. Physically, when the shear rate is decreased, the aggregates get larger (more inflated). They finally touch each other and form an infinite spanning network at rest with $\varphi_{m,a}\sim 1$ and the internal volume fraction of aggregates equal to the particle volume fraction in the suspension: $\varphi_i \approx \varphi$. In this sense, the model predicts the threshold stress, σ_{th}, below which the suspension is jammed when the applied stress is decreased. Thus, the proposed aggregation scenario is, to some extent, equivalent to the network failure scenario of the yield stress. The difference lies in opposite directions of reaching the yield point. The network scenario considers a network breakup at increasing stress, while the aggregation scenario deals with the jamming at decreasing stress. If one assumes a reversible process of the network destruction (at increasing stress) and construction (at decreasing stress), both scenarios give the same magnitude σ_{th}, which can be assimilated to the yield stress. Absence of distinguishable flow curve hysteresis in our experiments allows us to use the value σ_{th} as an estimate of the yield stress σ_Y.

The condition $\varphi_a \approx \varphi_{m,a}\sim 1$ is reached when the term in square brackets of Eqs. (8) and (15) tends to zero and the relative viscosity η_a^r diverges. Setting this term to zero and Φ_1 to unity, the following expression for the yield stress is obtained:

$$\sigma_Y = \frac{\varphi^2}{1-(\varphi/\varphi_{m,i})^2}\frac{32F_A r}{5\pi^2 d^2} \tag{27}$$

To analyze the concentration behavior of the yield stress, we plot in Fig. 8 the theoretical and experimental dependencies of the suspension yield stress on particle volume fraction in log-log scale for the two PA suspensions used in experiments. At low concentrations, the theoretical curves are linear in the log-log scale with a slope equal to two corresponding to the φ^2-behavior established by Eq. (27) at $\varphi << \varphi_{m,i}$. At higher φ, the concentration dependence becomes stronger leading to a divergence of the yield stress as the particle volume fraction approaches the upper limit of the colloidal glass state $\varphi \to \varphi_{m,i} = 5.4/r$. The agreement between the theory and the experiments is rather poor likely because of a poor precision of the yield tress determination at the stress values as low as 0.1 Pa. In particular, experiments show a stronger concentration behavior of the yield stress of PA suspensions, $\sigma_Y \propto \varphi^{4\pm 0.8}$, as compared to the model predictions. This discrepancy likely comes from the fact that the adhesive force F_A may increase with the particle volume fraction φ, such that the predicted behavior, $\sigma_Y \propto \varphi^2 F_A/(1-(\varphi/\varphi_{m,i})^2)$, would be stronger then quadratic. In fact, an applied macroscopic stress σ_Y is transmitted to contact points and press

the fibers to each other. The adhesive force acts on the roughness scale, $h_A \sim h_R$, so that a stronger transmitted stress at higher φ could lead to stronger interlocking of surface asperities at the contact point and, consequently to lower effective separations h_A and higher adhesive forces $F_A \propto h_A^{-2}$ [Eq. (11)]. Unfortunately, we are unable to confirm this explanation at the present time.

Strong concentration effects on the yield stress have been previously observed in: (a) CNT suspensions with $\varphi^{2.1}$ to $\varphi^{3.2}$ behaviors for aspect ratios r=80 and 1200, respectively [77, 78], (b) nanofibrillated cellulose suspensions with $\varphi^{3.1}$ [11], and (c) flexible pulp fiber suspensions with $\varphi^{2.5}$ to φ^{5}-trend found between the experiments, theory and simulations [20, 21, 28, 79]. As already mentioned, the existence of a yield stress and the strong concentration effects for attractive flexible fiber suspensions are explained mostly by the interplay between the fiber bending and inter-fiber solid friction. In repulsive systems, the yield stress is interpreted as a stress required to overcome repulsive colloidal forces and continuously extract the fibers from the current network configuration to the new one [11]. The $\varphi^{3.1}$ behavior in these systems comes from the decrease in the Debye length and the variations in electrostatic potential with increasing concentration.

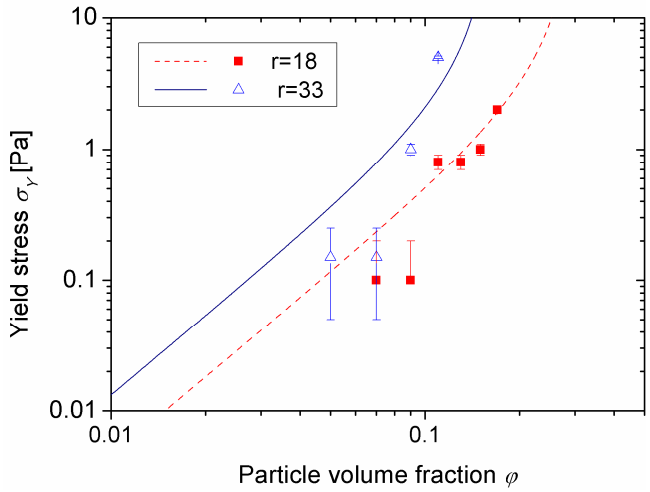

Fig. 8. Theoretical and experimental dependencies of the yield stress on the particle volume fraction for PA fibers with r=18 and r=33. The values of the adjustable parameter F_A summarized in Table IV of Appendix D were used for the yield stress calculations. The symbols stand for the experiments and lines –for the theory

Finally, notice that our previous model, considering only non-aggregated fibers with frictional contacts, predicted a purely Bingham behavior with a yield stress given by the expression [36]:

$$\sigma_Y = \frac{16}{\pi^2}\varphi^2 \frac{F_A r}{d^2} \tag{28}$$

with $F_A = \mu F$, μ - friction coefficient and F - the van der Waals force given by Eq. (11). Both models give the same dimensional scaling for the yield stress, $\sigma_Y \propto F_A r / d^2$ and the same concentration behavior $\sigma_Y \propto \varphi^2$ at low particle volume fractions, $\varphi << \varphi_{m,i}$. However, at higher volume fractions, the present aggregation model provides a stronger concentration behavior $\sigma_Y \propto \varphi^2 F_A /(1-(\varphi/\varphi_{m,i})^2)$ than the model of non-aggregated fibers with $\sigma_Y \propto \varphi^2$ at any φ. Notice that the previous model [36] does not reproduce at all the shape of the experimental flow curves of PA suspensions [Fig. 6] and gives zero yield stress in absence of solid friction between fibers. Introduction of aggregation in the present model allows us to obtain a reasonable agreement with experiments and reproduce a shear thinning without solid friction.

V. Conclusions

This work is focused on shear thinning behavior of rigid non-Brownian fiber suspensions under the action of adhesive interactions between particles. Rheological experiments have been conducted with neutrally buoyant PA fiber suspensions. For the sake of comparison, the experimental data of Natale *et al*. [34] on suspensions of untreated multiwall CNTs dispersed in a Newtonian epoxy resin have also been analyzed. The experimental results can be summarized as follows:

1. The steady-state flow curves of both PA and CNT fiber suspensions show a significant shear thinning with a decrease of the viscosity attaining two-to-three orders of magnitude when the shear rate is increased from 0.1 to 100 s^{-1}. The degree of shear thinning has been found to increase with particle concentration, in accordance with experimental results of Mueller *et al*. [19].
2. A small yield stress has been detected in PA fiber suspensions in controlled-stress measurements. The measurements in controlled-rate mode were unable to confirm the existence of a yield stress in suspensions of relatively short CNT ($r \approx 36$) used in experiments of Natale *et al*. [34]. However, other authors report a non-negligible yield stress related to formation of a network in suspensions of longer nanotubes ($80 < r < 1200$) [77, 78].
3. Visualization experiments on PA suspensions reveal some spatial heterogeneity with denser domains separated by free fibers. The fibers belonging to these domains show a cooperative motion and some misalignment relatively to each other.

For a better understanding of these findings, a theoretical model has been developed allowing us to establish the relationship between the adhesive force between contacting fibers and the shear thinning behavior. The model assumes existence of transient aggregates whose size is assimilated to a correlation length $D \sim (1\text{-}2)l$ of experimentally observed spatial heterogeneities.

The model seems to capture the main experimental behaviors of PA and CNT suspensions:

1. The enhancement of the shear thinning with increasing particle volume fraction has been confirmed and explained by the fact that both the adhesive interactions and the fraction Φ_1 of aggregated fibers increase with the particle concentration.

2. A weak yield behavior of the PA fiber suspensions has been confirmed. According to our model, the yield stress comes from the liquid-solid transition as the aggregate concentration φ_a approaches the maximum packing limit $\varphi_{m,a}$ resulting in divergence of the viscosity as the shear rate goes to zero.

3. The model reproduces a much stronger shear thinning in CNT suspensions than in PA ones, which is explained by a stronger role of adhesive interactions between nanoscale CNT particles than between micron-sized PA fibers.

4. From a microscopic perspective, the short-ranged interactions between fibers are likely governed by two different length scales. Comparison between theoretical and experimental rheological response indicates that the interactions between free fibers are hydrodynamic with a characteristic length $h_H \sim d$, while the interactions between aggregated fibers are predominately adhesive (frictional or non-frictional) with $h_A << d$, where d is the fiber diameter.

Acknowledgements

The authors are grateful to Région Provence Alpes Côte d'Azur for funding one of us, to "La société nouvelle le flockage" for supplying the fibers. We are grateful to Dr. E.Peuvrel-Disdier and Dr. R. Castellani of Ecole des Mines de Paris for visualization experiments and to Prof. P.J. Carreau, Prof. M.C. Heuzey and Dr. G. Natale of Polytechnique Montréal for providing the data on CNT suspensions.

Appendix A. Cohesive strength of the aggregates

Let us suppose that the fracture region is localized in a plane layer of a width equal to the fiber length l and created by cutting the aggregate by two planes parallel to the middle fracture plane and separated from it by a distance $l/2$ [Fig.1b]. Let the orientation of two contacting fibers inside the aggregates described by unit vectors the unit vectors $\mathbf{p}^{\alpha}$ and $\mathbf{p}^{\beta}$ [Fig. 1c] and the direction of the aggregate rupture – by a unit vector **e** oriented along the extension axis [Fig. 1b]. During the aggregate break-up, two possibilities of the contact rupture are considered on the basis of Assumption (5), as schematized in Fig. 9. In the case of normal rupture, the fibers are separated from each other along a unite vector **n** perpendicular to their contact surface. Then, the cohesive force is the normal adhesive force $\mathbf{F}_n$ aligned with **n**. In the case of tangential rupture, the fibers slide along each other. In such a case, the cohesive force is the friction force $\mathbf{F}_\tau$ whose absolute value is proportional to the normal adhesive force, $F_\tau = \mu F_n$ [Eq. (3)] and whose orientation is opposed to the direction of

motion of the contact point. This direction is characterized by a unit vector **τ**, which belongs to the plane $\alpha\beta$ (formed by the contacting fibers α and β) and oriented along the projection of the unit vector **e** onto the plane $\alpha\beta$ [Fig. 9]. Let Θ be the angle that the unit vector **e** makes with the unit vector **n**. For a given contact point, the projection of the cohesive force onto the extension axis reads:

$$F_1 = \begin{cases} -F_n \left|\cos\Theta\right|, & \text{normal rupture;} \\ -\mu F_n \left|\sin\Theta\right|, & \text{tangentional rupture} \end{cases} \tag{A-1}$$

Here the minus sign appears because the cohesion force is opposed to the direction of the aggregate rupture. The *e*-component (along the extension axis) of the total cohesion force exerted on a test fiber α by all the neighboring fibers β is found by weighing the cohesion force [Eq. (A-1)] by the contact probability dP_A:

$$F_\alpha = \int F_1 dP_A \tag{A-2}$$

$$dP_A = 2n_i(d+h_A)\left|\mathbf{p}^\alpha \times \mathbf{p}^\beta\right| ds_\alpha ds_\beta \psi_\beta d\mathbf{p}^\beta \tag{A-3}$$

where n_i is the number fraction of fibers inside the aggregates.

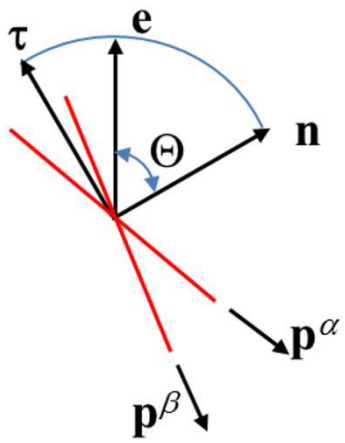

Fig. 9. Sketch for determination of the contact rupture

The resultant cohesive force (cohesive strength) acting on all N fibers situated in the fracture region is proportional to the product of the number of fibers N by the force F_α averaged over all possible orientations of the test fiber "α":

$$\begin{aligned} F_c &= \frac{1}{2} N \int F_\alpha \psi_\alpha d\mathbf{p}^\alpha = N n_i (d+h_A) \int_{-l/2}^{l/2} ds_\alpha \int_{-l/2}^{l/2} ds_\beta \int_{\mathbf{p}^\alpha} \psi_\alpha d\mathbf{p}^\alpha \int_{\mathbf{p}^\beta} \left|\mathbf{p}^\alpha \times \mathbf{p}^\beta\right| F_1 \psi_\beta d\mathbf{p}^\beta = \\ &= -N n_i (d+h_A) l^2 F \times \begin{cases} \left\langle \left|\cos\Theta\right| \right\rangle, & \text{normal rupture;} \\ \mu \left\langle \left|\sin\Theta\right| \right\rangle, & \text{tangential rupture} \end{cases} \end{aligned} \tag{A-4}$$

where ψ_α is the angular distribution function of the test fibers α; F is the value of the normal colloidal force F_n for the angle between two fibers equal to $\delta=\pi/2$ [cf. Eq. (10)]; the factor (1/2) is introduced in order to avoid double counting of the contact force acting in the contact point of a pair of fibers; the magnitudes $|\cos\Theta|$ and $|\sin\Theta|$ are averaged according to the rule $\langle X\rangle = \int_{\mathbf{p}^\alpha}\psi_\alpha d\mathbf{p}^\alpha \int_{\mathbf{p}^\beta}\psi_\beta X(\mathbf{p}^\alpha,\mathbf{p}^\beta)d\mathbf{p}^\beta$ and are found as function of the orientation vectors $\mathbf{p}^\alpha$, $\mathbf{p}^\beta$ and $\mathbf{e}$ by the following expressions:

$$|\cos(\Theta)| = \frac{\left|\mathbf{e}\cdot(\mathbf{p}^\alpha\times\mathbf{p}^\beta)\right|}{\left|\mathbf{p}^\alpha\times\mathbf{p}^\beta\right|}, \quad |\sin\Theta| = \left[1-\left(\frac{\mathbf{e}\cdot(\mathbf{p}^\alpha\times\mathbf{p}^\beta)}{\left|\mathbf{p}^\alpha\times\mathbf{p}^\beta\right|}\right)^2\right]^{1/2} \qquad \text{(A-5)}$$

The average values $\langle|\cos\Theta|\rangle$ and $\langle|\sin\Theta|\rangle$ depend on the orientation state inside the aggregates and are summarized in Table III.

Table III. Values of $\langle|\cos\Theta|\rangle$, $\langle|\sin\Theta|\rangle$ and ξ for different considered cases

Orientation state	Sketch	$\langle\lvert\cos\Theta\rvert\rangle$	$\langle\lvert\sin\Theta\rvert\rangle$	Rupture scenario	$\xi = F_A / F$
Isotropic		$\frac{1}{2}$	$\frac{\pi}{4}$	normal	$\frac{1}{2}$
Isotropic		$\frac{1}{2}$	$\frac{\pi}{4}$	tangential	$\frac{\pi}{4}\mu$
Nearly aligned along **e**		$O(r^{-1})$	≈ 1	tangential	μ
Nearly aligned, perpendicular to **e**		≈ 1	$O(r^{-1})$	normal	1

To get the final expression for the cohesive strength, we find the number of fibers N and their number density n_i in the fracture region as follows:

$$n_i = \frac{\varphi_i}{V_f} = \frac{4\varphi_i}{\pi d^2 l}; \quad N = n_i V_{fracture} \approx \frac{4\varphi_i}{\pi d^2 l}\frac{\pi D^2 l}{4} = \varphi_i \frac{D^2}{d^2}, \qquad \text{(A-6)}$$

where V_f is the fiber volume, φ_i is the internal volume fraction of aggregates, and $V_{fracture}$ is the volume of the fracture zone of a thickness *l* and diameter *D* [Fig.1b].

Substituting Eq. (A-6) into Eq. (A-5) and using appropriate values of $\langle|\cos\Theta|\rangle$ and $\langle|\sin\Theta|\rangle$ [Table III], we get the final expression [Eq. (12)] for the cohesive strength, in which the inter-fiber gap h_A is neglected before the fiber diameter *d*. The effective adhesive force $F_A = \xi F$ introduced into this expression generalizes different considered cases through the multiplier ξ whose values are summarized in Table III, as function of the chosen contact rupture scenario and orientation state.

For realistic values $0.3 < \mu < 0.5$ of the friction coefficient, the cohesive force between fibers, *F* or μF, is of the same order of magnitude for both rupture mechanisms.

To check whether the fiber orientation strongly influences the cohesive strength of the aggregates, in addition to the assumed isotropic state (Assumption 7.1) we consider a nearly aligned state, in which case the condition $\langle\sin\delta\rangle = \langle|\mathbf{p}^\alpha \times \mathbf{p}^\beta|\rangle \geq r^{-1}$ holds and the equations (10) and (A.3) are still valid [60]. We assume that the aggregate rupture occurs when the fibers are either aligned with the extension axis or perpendicular to it. In the first case, the fibers slide along extension axis during the aggregate break-up. This corresponds to the tangential rupture scenario. In the second case, the fibers move apart in the direction normal to the contact surface; normal rupture scenario is expected [cf. sketches in Table III]. In both these cases of the aligned orientation, the cohesive strength of the aggregate appears to be very close to the one found for isotropic orientation. This is because: (a) the product of the number of contacts by the adhesive force of a pair of fibers is independent of the orientation scalar $f_1 = \langle|\mathbf{p}^\alpha \times \mathbf{p}^\beta|\rangle$ [cf. Appendix B], and (b) $\langle|\cos\Theta|\rangle$ and $\langle|\sin\Theta|\rangle$ vary between ½ and 1 for different orientations, while the value $O(r^{-1})$ is excluded from consideration because it does not contribute to the cohesive strength.

A relatively small variation of ξ (which is of the order of unity) allows us to apply the obtained results to intermediate states where (1) normal rupture of contacts coexist with tangential rupture during the aggregate break-up; and (2) the orientation state inside the aggregate is arbitrary. In those cases, an appropriate value of the parameter ξ, that fits into the range $\min(1/2, \pi\mu/4) \leq \xi \leq \max(1, \mu)$, should be chosen.

Note finally that if the aggregate size is of the order of the fiber length, the whole aggregate is expected to be disintegrated into individual fibers rather than be broken in parts. However, the number of ruptured contacts and, consequently, the aggregate cohesive strength are still correctly estimated using the above considered fracture scenario.

Appendix B. Fiber connectivity

The fiber connectivity in both populations is characterized by the average number of contacts per fiber, called the coordination number and defined by the expression [11, 80]: $Z = 4\varphi\left(1+h/d\right)^2\left(2f_1 r/\left[\pi(1+h/d)\right]+f_2+1\right)$, where $f_1 = \left\langle\left|\mathbf{p}^\alpha \times \mathbf{p}^\beta\right|\right\rangle$, $f_2 = \left\langle\left|\mathbf{p}^\alpha \cdot \mathbf{p}^\beta\right|\right\rangle$, h=h_H for free fibers and h=h_A for aggregated fibers. More precisely, the coordination number affects the viscosities through the term $Z/f_1 \approx 8\varphi r(1+h/d)/\pi$ obtained at $r >> 1$. The orientation scalar f_1 disappears while averaging adhesive and lubrication forces over the contact probability, because the product of each of this force with the contact probability is independent of $\left|\mathbf{p}^\alpha \times \mathbf{p}^\beta\right|$, as inferred from Eqs. (4), (5), (10) and (A-3). The coordination number inside the aggregates should be higher than the percolation threshold $Z_p \approx 1.4$ [81]. This constraint imposes the lower bounds of suspension concentration at which our model is still valid: $\varphi_{\min} \approx 0.02$ at r=18 and $\varphi_{\min} \approx 0.01$ at r=33. Our PA suspensions respect these bounds. The CNT suspensions characterized by Khalkhal *et al*. (2011) [37] and used for comparison with our model are quite polydisperse, some CNTs attain the aspect ratio of the order of 100 at the mean value r=36. Therefore their coordination number is likely underestimated.

Appendix C. Sticking probability α_0 [Eq. (26)].

The fibers are supposed to stick after collision if the adhesive force produces a torque $T_A \sim F_A s/f_1 \sim F_A sr$ strong enough to overcome a hydrodynamic torque $T_H \sim \eta l^3\omega/\ln(2r) \sim \sigma l^3/(r\ln(2r))$, otherwise the adhesive contact may be easily ruptured. Here, s is the distance along the fiber major axis between the fiber center of mass and the contact point [cf. Fig. 1c]; $f_1 = \left\langle\left|\mathbf{p}^\alpha \times \mathbf{p}^\beta\right|\right\rangle \sim r^{-1}$ [36]; $\omega \sim \dot\gamma/r$ is an average angular velocity of the fiber; the viscosity of the suspending liquid η_0 is again replaced by the suspension viscosity η in order to account for hydrodynamic interactions between fibers, and the product $\eta\dot\gamma = \sigma$ refers to the applied shear stress. The condition $T_A \geq T_H$ implies that the fibers stick when the contact point is situated in the interval $s_0 \leq s \leq l/2$, that corresponds to the sticking probability $\alpha_0 \sim 1 - 2s_0/l$, where the critical distance $s_0 \sim \sigma d^2 l/(F_A \ln(2r))$ is given by the equilibrium of torques. This approach applies well for low shear regime but likely underestimates the contact probability at high shear producing negative values of α_0 above some critical stress. To avoid this inconsistency and impose a smooth variation of α_0 from unity at low shear stresses to zero at infinite stresses, we replace $\alpha_0 \sim 1 - 2s_0/l$ by $\alpha_0 \sim e^{-2s_0/l}$. The last expression reduces to the initially derived low shear limit at $2s_0/l << 1$ and takes the final form of Eq. (26), discarding numerical multipliers and making use of Eq. (2) for the aggregation parameter N_A.

Appendix D. Adjustable parameters and the gaps h_H and h_A

The set of the adjustable parameters (h_H, F_A, κ) is summarized in Table IV. The values of the first adjustable parameter h_H (the gap between the free fibers) for the PA fibers were chosen similar to those used for the fit of the concentration dependencies of the high-shear viscosity [cf. Fig. 5].

Table IV. Adjustable parameters of the model and different length scales

Sample	Effective adhesive force F_A [N]	Correction factor [Eq.(23)] κ	Length scales			
			Fiber diameter d [μm]	Roughness h_R [μm]	Gap (hydro) h_H [μm]	Gap (adhesive) h_A [μm]
PA, r=18	3.0×10^{-9}	1	27.8±0.5	$(5\pm2)\times10^{-3}$	9.0	2.8×10^{-3}
PA, r=33	1.5×10^{-9}	1	15.2±0.5	$(14\pm4)\times10^{-3}$	6.0	3.0×10^{-3}
CNT	2.5×10^{-12}	0.05	0.014*	N/A	8.0×10^{-3}	2.2×10^{-3}

* Peak value of the CNT diameter

The values of the second adjustable parameter, F_A, allow us to estimate the gap h_A between aggregated fibers. Assuming van der Waals adhesive interaction, the value of h_A is obtained from Eq. (10), in which the Hamaker constant is of the order $A\sim10^{-20}$ J for both PA and CNT suspensions (cf. Sec. C of Supplemental Materials) [42] and F is replaced by $F_A=\xi F$ taking into account that the multiplier ξ is of the order of unity [cf. Appendix A].

It is worth noticing that, the chosen values of our adjustable parameter $F_A\sim(1.5-3)\times10^{-9}$ N approach the values of the adhesive force measured by Chaouche and Koch [17] for PA fibers dispersed either in a silicon oil, $F\sim10^{-8}$ N, or in a water-glycerol solution, $F\sim10^{-7}$ N, and having nearly the same size as the ours.

Finally, the dimensionless correction factor κ, appearing in Eqs. (24), (25) for fiber fractions Φ_1 and Φ_2, is set to unity ($\kappa=1$) for PA fibers of both aspect rations (r=18 and 33). This parameter is set to 0.05 for CNT suspensions – a value twenty times lower than the one used for PA fibers. A lower parameter $\kappa=k_2/k_1$ stands for higher aggregation rate or lower destruction rate [cf. Eq.(23)] in CNT suspensions. This is qualitatively consistent with our previous argument on more important role of colloidal interactions between nanoscale CNT particles as compared to micron-sized PA fibers [Section IV-C].

Appendix E. Low-shear concentration behavior

At low shear rates, the suspensions are expected to be highly aggregated, and their concentration behavior is expected to differ from that shown on Fig. 5 for high shear rates. In order to better appreciate the concentration effect on the low shear viscosity, the ratio $\eta^r(0.1\ \mathrm{s}^{-1})/\eta^r(100\ \mathrm{s}^{-1})$ of the low shear viscosity to the high shear viscosity is plotted against particle volume fraction in Fig. 10 for both the PA (at r=18 and 33) and CNT suspensions. The viscosity ratio appears to be a growing function of the particle concentration

for the three suspensions meaning that the suspensions are much more shear-thinning at high concentrations than at low concentrations. Such concentration enhancement of the shear thinning comes from the synergy of the two following effects: (a) adhesive interactions between fibers give a stronger than linear concentration behavior of the suspension viscosity [cf. Eq. (15)]; (b) the fraction Φ_1 of aggregated fibers monotonically increases with the particle concentration [cf. Eq. (24)] providing a further increase in viscosity.

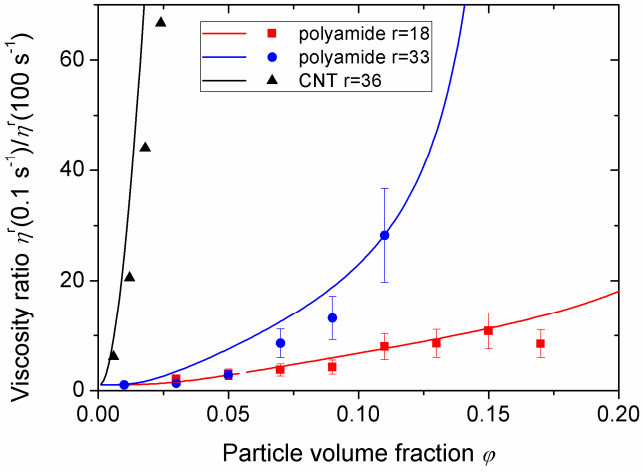

Fig. 10. Theoretical and experimental dependences of the ratio of low-shear-to-high-shear viscosity $\eta^r(0.1\ s^{-1})/\eta^r(100\ s^{-1})$ on particle volume fraction. Symbols – experiment, solid lines – theory. The values of the adjustable parameters are summarized in Table IV of Appendix D.

In order to better illustrate the second effect, the theoretical dependency of the fraction Φ_1 of aggregated fibers on the particle volume fraction is plotted in Figure 11 for two PA suspensions at a shear rate $\dot{\gamma} = 0.1\ s^{-1}$.

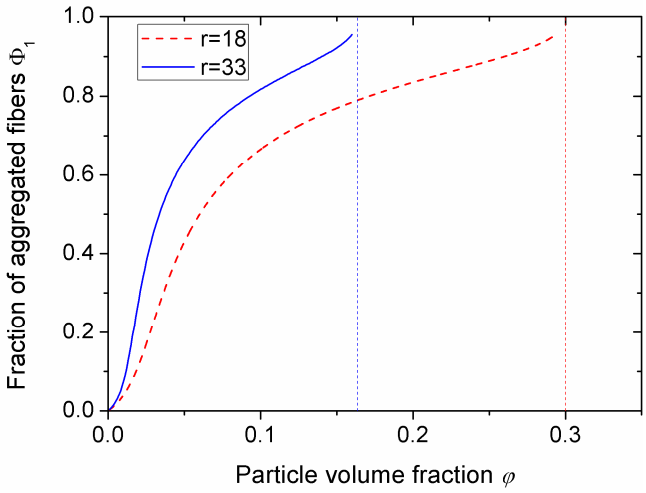

Fig. 11. Theoretical dependences of the fraction of aggregated fibers on the particle volume fraction of PA suspensions at $\dot{\gamma} = 0.1\ s^{-1}$. The vertical dashed lines stands for the upper concentration limit $\varphi_{m,i} = 0.3$ and $\varphi_{m,i} \approx 0.16$ for PA fiber suspensions with r=18 and 33, respectively. The values of the adjustable parameters are summarized in Table IV in Appendix D.

Figure 11 shows that the fraction Φ_1 of aggregated fibers progressively increases from zero to unity between the infinite dilution limit $\varphi \to 0$ and the upper concentration bound $\varphi \to \varphi_{m,i} = 5.4/r$ assumed to be the upper limit of the colloidal glass state.

References

[1] Agassant J.F., P. Avenas, J.P. Sergent, B. Vergnes, and M. Vincent. « *La mise en forme des matières plastiques* » (Lavoisier, TEC & DOC, 1996).

[2] Jeffery, G. B. "The motion of ellipsoidal particles immersed in a viscous fluid". Proc. Royal Soc. London A **102**, 161-179 (1922).

[3] Larson R. G., "*The Structure and Rheology of Complex Fluids*" (Oxford University Press, 1999).

[4] Petrie C. J. The rheology of fibre suspensions. J. NonNewt. Fluid. Mech. **87**, 369-402 (1999)

[5] Djalili-Moghaddam, M., and Toll S. "A model for short-range interactions in fibre suspensions". J. NonNewt. Fluid. Mech. **132**, 73-83 (2005).

[6] Férec, J., Ausias, G., Heuzey, M. C., and Carreau, P. J. "Modeling fiber interactions in semiconcentrated fiber suspensions." J. Rheol. **53**, 49-72 (2009)

[7] Sundararajakumar, R. R., and Koch, D. L. "Structure and properties of sheared fiber suspensions with mechanical contacts". J. NonNewt. Fluid Mech. **73**, 205-239 (1997).

[8] Lindström, S. B., and Uesaka, T. A., "Numerical investigation of the rheology of sheared fiber suspensions", Phys. Fluids **21**, 083301 (2009).

[9] Snook, B., Davidson, L. M., Butler, J. E., Pouliquen, O., and Guazzelli, E. "Normal stress differences in suspensions of rigid fibres". J. Fluid Mech. **758**, 486-507 (2014).

[10] Quemada, D., and Berli, C. "Energy of interaction in colloids and its implications in rheological modeling". Adv. Coll .Int. Sci., **98**, 51-85 (2002)

[11] Martoïa, F., Dumont, P. J. J., Orgéas, L., Belgacem, M. N., and Putaux, J. L. « Micro-mechanics of electrostatically stabilized suspensions of cellulose nanofibrils under steady state shear flow". Soft Matter **12**, 1721-1735 (2016).

[12] Raghavan, S. R., and Douglas, J. F. "The conundrum of gel formation by molecular nanofibers, wormlike micelles, and filamentous proteins: gelation without cross-links?" Soft Matter **8**, 8539-8546 (2012).

[13] Solomon, M. J., and Boger, D. V. "The rheology of aqueous dispersions of spindle-type

colloidal hematite rods", J. Rheol. **42**, 929-949 (1998).

[14] Michot, L. J., Baravian, C., Bihannic, I., Maddi, S., Moyne, C., Duval, J. F., Levitz P., and Davidson, P. "Sol− Gel and Isotropic/Nematic Transitions in Aqueous Suspensions of Natural Nontronite Clay". Influence of Particle Anisotropy. 2. Gel Structure and Mechanical Properties," Langmuir **25**, 127-139 (2008).

[15] Wierenga, A., Philipse, A. P., Lekkerkerker, H. N., and Boger, D. V. "Aqueous dispersions of colloidal boehmite: Structure, dynamics, and yield stress of rod gels", Langmuir **14**, 55-65 (1998)

[16] Mongruel, A., and Cloitre, M. "Shear viscosity of suspensions of aligned non-Brownian fibres". Rheol. Acta **38**, 451-457 (1999).

[17] Chaouche, M., and Koch, D. L. "Rheology of non-Brownian rigid fiber suspensions with adhesive contacts". J. Rheol. **45**, 369-382 (2001).

[18] Bergström, L. "Shear thinning and shear thickening of concentrated ceramic suspensions." Colloids and Surfaces A **133**, 151-155 (1998).

[19] Mueller, S., Llewellin, E. W., and Mader, H. M. "The rheology of suspensions of solid particles." Proc. Royal Soc. London A **466**, 1201-1228 (2009).

[20] Bennington, C. P. J., Kerekes, R. J., and Grace, J. R. "The yield stress of fibre suspensions". Canad. J. Chem. Eng., **68**, 748-757 (1990).

[21] Cui, H., and Grace, J. R. "Flow of pulp fibre suspension and slurries: A review". Int. J. Multiphase Flow, **33**, 921-934 (2007).

[22] Song, Y. S., and Youn, J. R." Influence of dispersion states of carbon nanotubes on physical properties of epoxy nanocomposites", Carbon **43**, 1378-1385. (2005).

[23] Fan, Z., and Advani, S. G. "Rheology of multiwall carbon nanotube suspensions", J.Rheol. **51**, 585-604 (2007).

[24] Wolf, B., White, D., Melrose, J. R., and Frith, W. J. "On the behaviour of gelled fibre suspensions in steady shear". Rheol. Acta **46**, 531-537 (2007).

[25] Schmid, C. F., and Klingenberg, D. J. "Mechanical flocculation in flowing fiber suspensions", Phys. Rev. Lett. **84**, 290-293 (2000).

[26] Switzer III L. H., and Klingenberg, D. J. "Flocculation in simulations of sheared fiber suspensions". Int. J. Multiphase Flow **30**, 67-87 (2004).

[27] Toll, S., and Månson, J. A. E. "Dynamics of a planar concentrated fiber suspension with non-hydrodynamic interaction", J. Rheol. **38**, 985-997 (1994).

[28] Servais, C., Månson, J. A. E., and Toll, S. "Fiber–fiber interaction in concentrated

suspensions: Disperse fibers". J. Rheol. **43**, 991-1004 (1999).

[29] Keshtkar M., MC Heuzey, and PJ Carreau. "Rheological behavior of fiber-filled model suspensions: effect of fiber flexibility," J. Rheology **53**, 631–650 (2009).

[30] Ma, W. K. A., Chinesta, F., Ammar, A., and Mackley, M. R. "Rheological modeling of carbon nanotube aggregate suspensions", J. Rheol. **52**, 1311-1330 (2008)

[31] Chinesta F., "From Single-Scale to Two-Scales Kinetic Theory Descriptions of Rods Suspensions," Archives of Computational Methods in Engineering **20**, 1-29 (2013)

[32] Abisset-Chavanne, E., Mezher, R., Le Corre, S., Ammar, A., and Chinesta, F. "Kinetic theory microstructure modeling in concentrated suspensions", Entropy, **15**, 2805-2832 (2013).

[33] Abisset-Chavanne, E., Chinesta, F., Ferec, J., Ausias, G., and Keunings, R. "On the multiscale description of dilute suspensions of non-Brownian rigid clusters composed of rods." J. NonNewt Fluid. Mech. **222**, 34-44 (2015)

[34] Natale G., M. C. Heuzey, and P. J. Carreau, G. Ausias and J. Férec, "Rheological Modeling of Carbon Nanotube Suspensions with Rod–Rod Interactions » AIChE J. **60**, 1476-1487 (2014)

[35] Férec J., A. Perrot and G. Ausias, "Toward modeling anisotropic yield stress and consistency induced by fiber in fiber-reinforced viscoplastic fluids", J.NonNewt. Fluid Mech. **220**, 69-76 (2015).

[36] Bounoua S., E. Lemaire, J. Férec, G. Ausias, A. Zubarev, and P. Kuzhir, "Apparent yield stress in rigid fibre suspensions: The role of attractive colloidal interactions," J. Fluid Mech. **802**, 611-633 (2016)

[37] Khalkhal, F., P. J. Carreau, and G. Ausias, Effect of flow history on linear viscoelastic properties and the evolution of the structure of multiwalled carbon nanotube suspensions in an epoxy. J. Rheol. **55**, 153-175 (2011).

[38] Genovese D. B., "Shear rheology of hard-sphere, dispersed, and aggregated suspensions, and filler-matrix composites." Adv. Coll. Int. Sci. **171-172**, 1-16 (2012)

[39] Rahatekar, S. S., Koziol, K. K. K., Butler, S. A., Elliott, J. A., Shaffer, M. S. P., Mackley, M. R., and Windle, A. H. "Optical microstructure and viscosity enhancement for an epoxy resin matrix containing multiwall carbon nanotubes". J. Rheol. **50**, 599-610 (2006).

[40] Vaccaro A. and G. Marrucci, "A model for the nonlinear rheology of associating polymers," J. Non-Newt. Fluid Mech. **92**, 261-273 (2000).

[41] Snabre P. and P. Mills, "I. Rheology of weakly flocculated suspensions of rigid

particles", Journal de Physique III **6**, 1811-1834 (1996)

[42] Supplemental Material: Deposit file 1 "Supplemental-Materials-R2.pdf" - Extension of the theoretical model to non-spherical aggregates (Sec. A); Comparison between erosion and rupture mechanisms (Sec. B); Experimental details (Sec. C)

[43]. Underhill P. T., J. P. Hernandez-Ortiz, and M. D. Graham, «Diffusion and spatial correlations in suspensions of swimming particles», Phys. Rev. Lett. **100**, 248101 (2008)

[44] Kerekes R.J., «Rheology of fibre suspensions in papermaking: An overview of recent research», Nord. Pulp Paper Res. J. 21, 100-114 (2006)

[45] Hartmann V., J. Vermant, E. Heinrich, J. Mewis and P. Moldenaers, "Effects of particles on the steady state and transient rheology of lyotropic hydroxypropylcellulose solutions", J.Rheol. **44**, 1417-1432 (2000).

[46] Bowden, F. P., and Tabor, D. "*The friction and lubrication of solids. Part. II.*" (Oxford University Press, London, 1964).

[47] Petrich, M. P., and Koch, D. L. "Interactions between contacting fibers", Phys. Fluids **10**, 2111-2113 (1998).

[48] Stone, T. W., Horstemeyer, M. F., Hammi, Y., and Gullett, P. M. "Contact and friction of single crystal nickel nanoparticles using molecular dynamics", Acta Materialia, **56**, 3577-3584 (2008).

[49] Fujita, M., and Yamaguchi, Y. "Simulation model of concentrated colloidal nanoparticulate flows". Phys. Rev. E **77**, 026706 (2008)

[50] Gallier, S., Lemaire, E., Peters, F., and Lobry, L. "Rheology of sheared suspensions of rough frictional particles", J. Fluid Mech., **757**, 514-549 (2014)

[51] Philipse, A. P., and Wierenga, A. M. "On the density and structure formation in gels and clusters of colloidal rods and fibers". Langmuir **14**, 49-54 (1998).

[52] Solomon, M. J., and Spicer, P. T. "Microstructural regimes of colloidal rod suspensions, gels, and glasses." Soft Matter **6**, 1391-1400 (2010).

[53] Guiraud, O., Orgéas, L., Dumont, P. J. J., and du Roscoat, S. R. "Microstructure and deformation micromechanisms of concentrated fiber bundle suspensions: An analysis combining X-ray microtomography and pull-out tests". J. Rheol., **56**, 593-623 (2012)

[54] Yamane Y., Y. Kaneda, and. M. Doi, "Numerical simulations of semi-dilute suspensions of rodlike particles in shear flow", J. NonNewt. Fluid. Mech. **54**, 405-421 (1994)

[55] Doi, M., and S. F. Edwards, "*The Theory of Polymer Dynamics*" (Oxford University Press, New York, 1986).

[56] Rahnama, M., Koch, D. L., and Shaqfeh, E. S. “The effect of hydrodynamic interactions on the orientation distribution in a fiber suspension subject to simple shear flow.” Phys. Fluids **7**, 487-506 (1995)

[57] Leal, L. G., and Hinch, E. J. “The effect of weak Brownian rotations on particles in shear flow,” J. Fluid. Mech. **46**, 685-703 (1971).

[58] Brenner H., “Rheology of a dilute suspension of axisymmetric Brownian particles”, Int. J. Multiphase Flow **1**, 195-341 (1974)

[59] Batchelor, G. K. “Slender-body theory for particles of arbitrary cross-section in Stokes flow”. J. Fluid Mech, **44,** 419-440 (1970).

[60] Hubbe M.A., “Flocculation and redispersion of cellulosic fiber suspensions: a review of effect of hydrodynamic shear and polyelectrolytes”, BioResources 2, 296-331 (2007)

[61] Björkman, U. “Break-up of suspended fibre networks”. Nordic Pulp and Paper Research Journal **18**, 32-37 (2003)

[62] Karppinen, A., Saarinen, T., Salmela, J., Laukkanen, A., Nuopponen, M., and Seppälä, J. “Flocculation of microfibrillated cellulose in shear flow”. Cellulose **19**, 1807-1819 (2012).

[63] Bagster, D. F., and Tomi, D. “The stresses within a sphere in simple flow fields.” Chem. Eng. Sci. **29**, 1773-1783 (1974)

[64] Van der Schoot, P., and Odijk, T. “Statistical theory and structure factor of a semidilute solution of rodlike macromolecules interacting by van der Waals forces”. J. Chem. Phys., **97**, 515-524 (1992).

[65] Russell, W. B., D. A. Saville, and W. R. Schowalter, “*Colloidal dispersions”* (Cambridge University Press, Cambrige, 1989)

[66] Vincze A., L. Demko, M. Vörös, M. Zrinyi, M. N. Esmail, and Z. Horvölgyi, “Two-Dimensional Aggregation of Rod-Like Particles: A Model Investigation”, J. Phys. Chem. B **106**, 2404-2414 (2002)

[67] Puisto A., Illa X., Mohtaschemi M., Alava M.J. “Modeling the viscosity and aggregation of suspensions of highly anisotropic nanoparticles”. Eur. Phys. J.E **35**, 1-7 (2012).

[68] Singh V., D. L. Koch, and A. D. Stroock, “Ideal Rate of Collision of Cylinders in Simple Shear Flow”, Langmuir **27**, 11813–11823 (2011)

[69] Van de Ven, T. G. M., “*Colloidal Hydrodynamics*” (Academic, London, 1989).

[70] Supplemental Material: Deposit file 2 “Video-aggregation.mp4”: MP4-video (best viewed in Google Chrome or Safari browsers) showing the shearing of the suspension of fiber volume fraction φ=0.05 and aspect ratio r=18 at 0.3 s^{-1} and at the gap between

moving plates fixed to three fiber lengths.

[71] Chapman B. "Shear-induced migration phenomena in concentrated suspensions" PhD Thesis, University of Notre Dame, US (1990)

[72] Chow, A. W., Sinton, S. W., Iwamiya, J. H., and Stephens, T. S. "Shear-induced particle migration in Couette and parallel-plate viscometers: NMR imaging and stress measurements". Phys. Fluids **6**, 2561-2576 (1994)

[73] Dbouk, T., Lobry, L., and Lemaire, E. "Normal stresses in concentrated non-Brownian suspensions". J. Fluid. Mech. **715**, 239-272 (2013).

[74] Ovarlez G., S. Rodts, X. Château, and P. Coussot, «Phenomenology and physical origin of shear localization and shear banding in complex fluids», Rheol. Acta **48**, 831–844 (2009).

[75] Saarikoski E, T. Saarinen, J. Salmela, and J. Seppälä, «Flocculated flow of microfibrillated cellulose water suspensions: an imaging approach for characterisation of rheological behaviour», Cellulose **19**, 647–659(2012)

[76] Suresh, L., and Walz, J. Y. "Effect of surface roughness on the interaction energy between a colloidal sphere and a flat plate". J. Coll. Int. Sci. **183**, 199-213 (1996)

[77] Rahatekar S.S., K.K. Koziol, S.R. Kline, E.K. Hobbie, J.W. Gilman, and A.H. Windle, "Length-dependent mechanics of carbon-nanotube networks," Adv. Mater. **21**, 874-878 (2009)

[78] Hobbie E.K., "Shear rheology of carbon nanotube suspensions", Rheol. Acta **49**, 323-334 (2010)

[79] Switzer III L. H. and D. J. Klingenberg, "Rheology of sheared flexible fiber suspensions via fiber-level simulations", J. Rheol. **47**, 759-778 (2003)

[80] Toll, S. "Note: On the tube model for fiber suspensions". J. Rheol. **37**, 123-125 (1993)

[81] Balberg I., C. H. Anderson, S. Alexander and N. Wagner, "Excluded volume and its relation to the onset of percolation", Phys. Rev. B **30**, 3933-3943 (1984)

Supplemental Materials:

- Deposit file 1 "Supplemental-Materials-R2.pdf" - Extension of the theoretical model to non-spherical aggregates (Sec. A); Comparison between erosion and rupture mechanisms (Sec. B); Experimental details (Sec. C)

- Deposit file 2 "Video-aggregation.mp4": MP4-video (best viewed in Google Chrome or Safari browsers) showing the shearing of the suspension of fiber volume fraction φ=0.05 and aspect ratio r=18 at 0.3 s^{-1} and at the gap between moving plates fixed to three fiber lengths.

Supplemental Materials

for the paper "Shear-thinning in concentrated rigid fiber suspensions: Aggregation induced by adhesive interactions" by Bounoua *et al*.

A. Extension of the theoretical model to non-spherical aggregates

The aggregate shape intervenes into the intrinsic viscosity $[\eta]$ appearing in Eqs. (8), (15) of the manuscript, as well as into the hydrodynamic force acting on the aggregate [Eq.(9)]. In this Section, we will define these quantities as function of the aggregate aspect ratio.

Let us suppose that the aggregates are prolate ellipsoids of revolution having a minor axis D, a major axis Dr_a and an aspect ratio r_a [Fig. S-1]. The aggregate is subjected to a linear shear field characterized by a shear rate $\dot{\gamma}$ and its orientation with respect to the laboratory reference frame xyz is described by the angles ϕ and θ. In the reference frame $x'y'z'$ related to the aggregate main axes, the shear field is characterized by the rate-of-strain tensor $\gamma'_{ik} = (1/2)(\partial v'_i/\partial x'_k + \partial v'_k/\partial x'_i)$. Suppose that the fracture plain of the aggregate is the middle plain perpendicular to its major axis z' and having a circular cross-sectional area πD^2. Thus, the rupture is assumed to occur along the major axis of the aggregate.

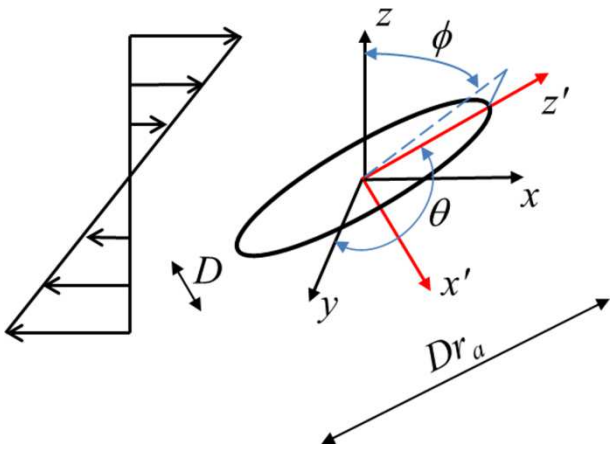

Fig. S-1. Sketch of the problem geometry

The distribution of hydrodynamic stress on the surface of the ellipsoid has been calculated by Jeffery (1922). The hydrodynamic rupture force along the major axis z' is obtained by integration of this stress over a half surface:

$$F_h = \pi\eta\dot{\gamma}D^2\left(\frac{2}{r_a} - \gamma_0 + \beta_0\right)C \qquad \text{(S-1a)}$$

$$C = \frac{1}{6}\frac{(2\gamma_0'' + \beta_0'')\hat{\gamma}_{zz}'}{(\beta_0'')^2 + 2\beta_0''\gamma_0''} \tag{S-1b}$$

$$\hat{\gamma}_{zz}' = \frac{\gamma_{zz}'}{\dot{\gamma}} = \sin^2\theta \sin\phi\cos\phi, \tag{S-1c}$$

$$\beta_0 = \frac{1}{r_a^2 - 1}\left[r_a - \frac{\ln\left(2r_a^2 - 1 + 2r_a\sqrt{r_a^2 - 1}\right)}{2\sqrt{r_a^2 - 1}} \right] \tag{S-1d}$$

$$\gamma_0 = -\frac{1}{r_a^2 - 1}\left[\frac{2}{r_a} + \frac{\ln\left(2r_a^2 - 1 - 2r_a\sqrt{r_a^2 - 1}\right)}{\sqrt{r_a^2 - 1}} \right] \tag{S-1e}$$

$$\beta_0'' = -\frac{1}{\left(r_a^2 - 1\right)^2}\left[3r_a + \frac{2r_a^2 + 1}{2\sqrt{r_a^2 - 1}} \ln\left(2r_a^2 - 1 - 2r_a\sqrt{r_a^2 - 1}\right) \right] \tag{S-1f}$$

$$\gamma_0'' = \frac{1}{4\left(r_a^2 - 1\right)^2}\left[r_a(2r_a^2 + 1) - \frac{4r_a^2 - 1}{2\sqrt{r_a^2 - 1}} \ln\left(2r_a^2 - 1 + 2r_a\sqrt{r_a^2 - 1}\right) \right] \tag{S-1g}$$

As expected, the hydrodynamic force is maximum, when the aggregate is situated in the shear plain xz (θ=π/2) and makes an angle ϕ=π/4 with the axis z [Fig. S-1]. This orientation corresponds to the following value of the zz-component of the rate of strain tensor: $\gamma_{zz}' = \dot{\gamma}/2$, as follows from Eq. (S-1c). In the case of the spherical aggregate (r_a=1), equation (S-1a) with the above components of γ_{ik}' reduces to the known result [Bagster and Tomi (1974)]:

$$F_{h,sph} = \frac{5\pi}{8}\eta\dot{\gamma}D^2 \tag{S-2}$$

This allows us to estimate the correction factor of the hydrodynamic force as:

$$\zeta' = \frac{F_h(r_a \geq 1)}{F_h(r_a = 1)} = \frac{8}{5}\left(\frac{2}{r_a} - \gamma_0 + \beta_0 \right) C \tag{S-3}$$

Fitting the $\zeta'(r_a)$ by simple functions we get the following correlation:

$$\zeta' \approx \begin{cases} r_a^{0.9}, & 1 \le r_a \le 4 \\ \dfrac{1}{3} r_a^{8/5}, & r_a > 4 \end{cases} \tag{S-4}$$

However, this factor will not likely correctly reflect the effect of the aggregate shape on its average rupture force. This is because elongated aggregates spend much more time aligned in the flow direction and will likely have less chance to be broken at $\phi=\pi/4$ than spherical aggregates, especially if the aggregate living time is smaller than the Jeffrey period. One way to account for this effect is to multiply the correction factor ζ' by the probability density ψ of finding the aggregate pointed along the extension axis ($\theta=\pi/2$, $\phi=\pi/4$) divided by the same probability for spherical aggregates (equal to $(4\pi)^{-1}$). This magnitude can be estimated in the limit of infinite Péclet numbers using the results of the work of Leal and Hinch (1971). The following correlation is obtained by fitting the results of that work with simple power-law functions:

$$4\pi\psi \approx \begin{cases} r_a^{-1/4}, & 1 \le r_a \le \sqrt{3} \\ 3 r_a^{-1}/2, & r_a > \sqrt{3} \end{cases} \tag{S-5}$$

Thus, the final approximate expression is obtained for the resultant correction factor for the hydrodynamic force:

$$F_h = \zeta F_{h,sph} \tag{S-6a}$$

$$\zeta = 4\pi\psi\zeta' \approx \begin{cases} r_a^{0.65}, & 1 \le r_a \le \sqrt{3} \\ 1.5 r_a^{-0.1}, & \sqrt{3} < r_a \le 4 \\ 0.5 r_a^{0.6}, & r_a > 4 \end{cases} \tag{S-6b}$$

The second parameter $[\eta]$ corresponds to the intrinsic viscosity of a dilute suspension of aggregates. In the limit of infinite Péclet numbers, the following correlation can be obtained from the values of $[\eta]$ tabulated in Brenner (1974):

$$[\eta] \approx \begin{cases} 2.5 + 0.0984 r_a, & 1 \le r_a \le 50 \\ 2 + \dfrac{0.315 r_a}{\ln(2r_a) - 1.5}, & r_a > 50 \end{cases} \tag{S-7}$$

These two corrections imply the following slight modifications of Eqs. (14), (15) and (27) of the manuscript:

$$\frac{1}{\varphi_i^2} = \frac{32 N_A r}{5\pi^2 \zeta} + \frac{1}{\varphi_{m,i}^2} \tag{S-8a}$$

$$\eta_a^{\,r} = \left[1 - \varphi\Phi_1\left(\frac{32F_A r}{5\pi^2\zeta\sigma d^2} + \frac{1}{\varphi_{m,i}^{\,2}}\right)^{1/2}\right]^{-[\eta]} \qquad \text{(S-8b)}$$

$$\sigma_Y = \frac{\varphi^2}{1-(\varphi/\varphi_{m,i})^2}\frac{32F_A r}{5\pi^2\zeta d^2} \qquad \text{(S-8c)}$$

The aggregates observed in our visualization experiments with polyamide fiber suspensions [see video in Supplemental Materials] have an aspect ratio varying between 1 and 3. The two above considered coefficients vary in the following ranges for these aspect ratios:

$$1 \le \zeta \le 1.4\,;\ 2.5 \le [\eta] \le 2.8 \ \text{ at } 1 \le r_a \le 3.5 \qquad \text{(S-9)}$$

These variations are not very significant compared to possible errors introduced by numerous assumptions of the model; it is therefore reasonable to consider spherical shape of the aggregates with $\zeta = 1$ and $[\eta] = 2.5$. However, the results of this section can be useful for other attractive suspensions developing more elongated aggregates.

B. Comparison between erosion and rupture mechanisms

To establish the dominant mechanism of the aggregate breakup, let us compare the shear stresses corresponding to aggregate destruction by both mechanisms.

In the case when the fiber is eroded from the aggregate surface, it experiences the maximum hydrodynamic force along the extension axis, as shown schematically in Fig. S-2. The hydrodynamic force acting on this fiber can be estimated as a product of the local normal stress $\sigma_{loc} = (5/2)\eta\dot{\gamma}$ on the aggregate surface and the fiber cross-sectional area $\pi d^2/4$:

$$F_h = \frac{5\pi}{8}\sigma d^2 \qquad \text{(S-10)}$$

where $\sigma = \eta\dot{\gamma}$ is the applied macroscopic stress.

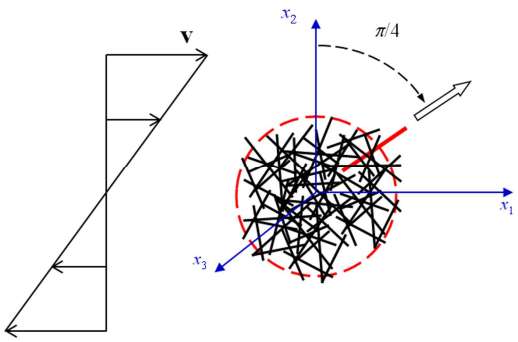

Fig. S-2. Erosion of a fiber from the aggregate surface. The eroded fiber is denoted a bold red line

The total cohesive force acting on a considered fiber "α" is the sum of all the attractive forces with neighboring fibers "β". It can be estimated as an integral of the single contact force F_1 over the contact probability dP_A (Eq. (A-3) of the manuscript):

$$F_c = \int F_1 dP_A = -2n_i(d+h_A)\int_0^{l/2} ds_\alpha \int_{-l/2}^{l/2} ds_\beta \int_{\mathbf{p}^\beta} \left|\mathbf{p}^\alpha \times \mathbf{p}^\beta\right| \frac{F_A}{\left|\mathbf{p}^\alpha \times \mathbf{p}^\beta\right|} \psi_\beta d\mathbf{p}^\beta \approx -n_i dl^2 F_A = -\frac{4}{\pi}\varphi_i F_A r\,, \quad \text{(S-11)}$$

where F_A is an effective adhesive force (cf. Appendix A of the manuscript) and $h_A \ll d$ is the mean separation between the fibers inside the aggregate. Here, we have assumed that only a half of the eroded fiber is immerged into the aggregate [Fig. S-2] that explains the zero value of the lower bound of the integral over s^α.

The fiber is supposed to be eroded when the equilibrium of forces (S-10) and (S-11) holds. This allows us to estimate the minimum applied stress required for the fiber erosion at a given internal volume fraction φ_i of the aggregate:

$$\sigma_e = \frac{32}{5\pi}\varphi_i \frac{F_A r}{d^2} \quad \text{(S-12)}$$

In the case of the aggregate fracture, the critical stress is obtained by the force balance acting on each half of the breaking aggregate. Setting to zero the sum of right-had sides of Eqs. (9) and (12) of the manuscript, we get the following expression for the rupture stress:

$$\sigma_r = \frac{32}{5\pi}\varphi_i^{\,2} \frac{F_A r}{d^2} \quad \text{(S-13)}$$

Comparison of Eqs. (S-12) and (S-13) show that both expressions differ only by a factor φ_i. Since in all the cases $\varphi_i < 0.3$ (cf. Fig. 7b of the manuscript), the rupture stress appears to be lower than the erosion stress, or, in other words, the fracture occurs at lower stresses and therefore is expected to be a dominant mechanism of the aggregate destruction.

C. Experimental details

The major part of this section is devoted to polyamide (PA) fiber suspensions. Thus, if not indicated, the estimated magnitudes concern these suspensions. For the meaning of the notations, please refer to the manuscript.

The fiber sedimentation time scale is estimated as the time required for the horizontal fiber to displace in the downward direction over its length [Chaouche and Koch (2001)]:

$$\tau_s \approx \frac{16\eta_0 l}{(\rho_f - \rho_0) g d^2 \ln 2r} \qquad \text{(S-14)}$$

Providing the density matching with a maximal error of $(\rho_f - \rho_0) = 2 \cdot 10^{-3}$ g/cm^3, the sedimentation time of PA fibers ($\tau_s \sim 7$ h) is estimated to be larger than the experimental time of the measurement interval for a given shear stress between two pre-shearing stages (see the measurement protocol in Sec. III-B of the manuscript).

The relative importance of the Brownian motion with respect to hydrodynamic interactions is described by the Péclet number [Larson (1999)]:

$$Pe \approx \frac{\pi \eta_0 l^3 \dot{\gamma}}{3 k_B T \ln 2r} \qquad \text{(S-15)}$$

where $k_B \approx 1.38 \cdot 10^{-23}$ J/K is the Boltzmann constant and T is the absolute temperature. The PA fibers are perfectly non-Brownian, as inferred from extremely high values of the Péclet number $Pe \approx 3 \cdot 10^7$ estimated in the worst case of the smallest shear rate $\dot{\gamma} = 10^{-2}$ s^{-1}.

The dimensionless effective stiffness of fibers is estimated as the ratio of the elastic bending stress to the hydrodynamic stress exerted on fibers using the following expression proposed by Switzer and Klingenberg (2003):

$$S_{eff} = \frac{E_Y I_0}{\eta_0 \dot{\gamma} l^4} = \frac{\pi E_Y}{64 \eta_0 \dot{\gamma} r^4} \qquad \text{(S-16)}$$

with $E_Y \approx 2$ GPa being the Young modulus of the PA fibers and $I_0 = \pi d^4 / 64$ - the cross-section area moment. Estimated values of the effective stiffness are presented in Table 1 of the manuscript. Estimations reveal the values $S_{eff} \gg 1$ in most cases of the present experiments. The PA fibers are therefore considered to be perfectly rigid. Note that in many other studies, the PA fibers either had a higher aspect ratio or were dispersed in a highly viscous fluid. In this case, the criterion $S_{eff} \gg 1$ did not hold and they were categorized as semi-flexible fibers [see for instance Keshtkar et al. (2009)]. The above estimations [Eq. (S-14)-(S-16)] allow us to validate the assumption (1) [Sec. II-A of the manuscript].

The ionic strength, I, of the suspending liquid and the thickness of the electric double layer, κ_e^{-1}, are estimated using the following expressions [van de Ven (1989)]:

$$I = \frac{1}{2} \sum c_i z_i^2 \qquad \text{(S-17a)}$$

$$\kappa_e^{-1} = \left(\frac{\varepsilon_0 \varepsilon k_B T}{2 N_0 e^2 I} \right)^{1/2} \qquad \text{(S-17b)}$$

where c_i is the molar concentration (in mol/m^3) of the ions of the valence z_i; $\varepsilon_0 \approx 8.85 \cdot 10^{-12}$ F/m - the dielectric permittivity of vacuum; $\varepsilon \approx 50$ – the relative dielectric permittivity of the oil-in-water mixture; $N_0 \approx 6 \cdot 10^{23}$ mol^{-1} – Avogadro number; $e \approx 1.6 \cdot 10^{-19}$ C – elementary charge; The values of I are reported in Table 2 of the Manuscript. At such high ionic strength (related to high salt concentration required for the density matching), the double layer thickness, κ_e^{-1}, appears to be less than 1 nm for both suspending liquids. The electrostatic interactions are expected to be completely screened and not to play significant role on the suspension rheology. PA suspensions are therefore fitted into the frames of our model developed for attractive interactions [assumption (3) of Sec. II-A of the Manuscript].

The Hamaker constant for PA fibers dispersed in UCON oil-in-water mixture was estimated using simplified Lifshitz theory applied to the case of non-retarded van der Waals interaction and completely screened electrostatic interaction [Russel et al. (1989)]:

$$A \approx \frac{3\hbar\omega_{UV}}{16\sqrt{2}} \frac{\left(n_f^{\,2} - n_s^{\,2}\right)^2}{\left(n_f^{\,2} + n_s^{\,2}\right)^{3/2}} \qquad \text{(S-18)}$$

where $\hbar = 1.055 \cdot 10^{-34}$ J·s is the Planck constant, $\omega_{UV} \approx 2.10^{16}$ rad/s – frequency of dominant relaxation in ultraviolet region for both PA and the suspending fluid, n_f=1.53±0.03 and n_s=1.38±0.03 - refractive indexes of PA fibers and the suspending fluid, respectively. Estimations give a value $A \sim 10^{-20}$ J for PA/UCON-water system.

The Hamaker constant for CNT dispersed in epoxy resin can be estimated using the same equation (S-18) with the values $\omega_{UV} \approx 7.2 \cdot 10^{15}$ rad/s, $n_f \approx 2.15$ and $n_s \approx 1.57$, as reported by Khalkhal et al. (2011). We also obtain the value $A \sim 10^{-20}$ J for CNT/epoxy composite. Note that a value $A \sim 10^{-19}$ J has been reported by Khalkhal et al. (2011), which is explained by an erroneous exponent used by in the denominator of Eq. (7) of that paper, namely ½ instead of 3/2 in Eq. (S-18). Also, we neglected the term depending on dielectric constants of the fibers and fluid because of its smallness, while this term is kept in the work of Khalkhal et al. (2011).

The Reynolds numbers on the scale of the flow (rheometer gap) and on the particle scale are estimated by the following expressions [Lindström and Uesaka (2009)]:

$$Re_{flow} = \frac{\rho_0 \dot{\gamma} b^2}{\eta}; \qquad Re_p = \frac{\rho_0 \dot{\gamma} d l}{\eta_0} \qquad \text{(S-19)}$$

Estimations give the following maximal values of the Reynolds numbers: $Re_{flow} \approx 8$ for the rheometer gap scale and $Re_p \approx 4 \cdot 10^{-3}$ for the particle scale. Both these values are below the limits $Re_{flow} \approx 360$ [Tillmark and Alfredsson (1992)] and $Re_p \sim 1$ [Happel and Brenner (1983)] of the laminar-to-turbulent transition on both considered scales. Thus

hypothesis (2) in Sec. II-A of the Manuscript is valid. Nevertheless, despite low values of Re, secondary flows may appear in torsional parallel plate geometry. The relative importance of these flows can be estimated by the ratio of the generated inertial pressure p_i to the shear stress [Mccoy and Dean (1971)]:

$$\frac{p_i}{\eta\dot{\gamma}} = \frac{0.15\rho_0(\dot{\gamma}b)^2}{\eta\dot{\gamma}} = 0.15Re_{flow} \qquad \text{(S-20)}$$

Within the experimental conditions, this ratio is lower or of the order of 1, meaning that, in most of our experiments, secondary inertial flows can be neglected.

The rheological measurements on PA suspensions conducted in a pool parallel plate geometry were subjected to two rheological corrections.

a) Moony correction

The shear stress is defined through the measurements of the applied torque *M*. The shear rate varies linearly from zero on the axis of symmetry to its maximum value at the rim, $\dot{\gamma}_R$ which is calculated from the measured rotational speed Ω. The following expressions were applied for the measured shear stress, shear rate and suspension viscosity [Macosco (1994)]:

$$\sigma_{app} = \frac{2M}{\pi R_{plate}{}^3}; \qquad \dot{\gamma}_R = \frac{R_{plate}\Omega}{b}; \qquad \eta_{app} = \frac{\sigma_{app}}{\dot{\gamma}_R} \qquad \text{(S-21)}$$

where the subscript "*app*" stands for the apparent shear stress or the apparent viscosity, which correspond exactly to the shear rate $\dot{\gamma}_R$ only in the case of a Newtonian fluid. In experiments, the apparent values σ_{app} and η_{app} are measured as function of $\dot{\gamma}_R$. Thus, to compare our experiments with the theory, the theoretical values of the shear stress σ and viscosity η are converted to the apparent ones using the following relationships [Macosco (1994)]:

$$\sigma_{app}(\dot{\gamma}_R) = \frac{4}{\dot{\gamma}_R{}^3}\int_0^{\dot{\gamma}_R}\dot{\gamma}^2\sigma(\dot{\gamma})d\dot{\gamma} \qquad \text{(S-22a)}$$

$$\eta_{app}(\dot{\gamma}_R) = \frac{\sigma_{app}}{\dot{\gamma}_R} = \frac{4}{\dot{\gamma}_R{}^4}\int_0^{\dot{\gamma}_R}\dot{\gamma}^3\eta(\dot{\gamma})d\dot{\gamma} \qquad \text{(S-22b)}$$

In order to use these relationships, we need to find theoretical dependences $\sigma(\dot{\gamma})$ and $\eta(\dot{\gamma})$ by solving the transcendental equation (15) of the manuscript with respect to σ and η, respectively, by using $\sigma = \eta\dot{\gamma} = \eta_0\eta_f{}^r\eta_a{}^r\dot{\gamma}$ [Eq. (16) of the manuscript].

Equation (S-22a) gives the following simple relationship between the apparent and the real yield stress for the parallel plate geometry:

$$\sigma_{Y,app} = \lim_{\dot{\gamma}_R \to 0} \left(\frac{4}{\dot{\gamma}_R^{\,3}} \int_0^{\dot{\gamma}_R} \dot{\gamma}^2 \sigma_Y d\dot{\gamma} \right) = \frac{4}{3} \sigma_Y \qquad \text{(S-23)}$$

All the rheological data reported in the manuscript for the PA suspensions are related to the apparent quantities. However the subscripts "*app*" and "*R*" are omitted for brevity. Notice that the above rheological correction does not apply to the results on CNT suspensions measured in a cone-plate geometry.

b) Correction for the pool geometry

The pool geometry shown in Fig. 3 of the manuscript gives overestimated values of the viscosity because of shearing of the suspension in the pool outside the gap. To estimate the necessary correction, the suspending liquid viscosity is measured both in the pool geometry as a function of the gap, $\eta_0^{\,pool}(b)$, and in conventional plate-plate geometry with a meniscus at the rim, $\eta_0^{\,p-p}$. The ratio of these viscosities is fitted by a linear function: $f(b) \equiv \eta_0^{\,pool}(b) / \eta_0^{\,p-p} = \alpha_1 + \alpha_2 b$. Then, the viscosity, $\eta^{pool}(b = 5 \text{ mm})$, of the PA suspensions is measured in the pool geometry with a gap equal to b=5 mm. Finally, assuming that the correction function $f(b)$ is the same for the fiber suspension and for the suspending liquid, the "true value" of the suspension viscosity η and of the relative viscosity η^r are deduced: $\eta = \eta^{pool}(b = 5 \text{ mm}) / f(b = 5 \text{ mm})$ and $\eta^r = \eta / \eta_0^{\,p-p}$.

References

Bagster, D. F., and Tomi, D. "The stresses within a sphere in simple flow fields." Chem. Eng. Sci. **29**, 1773-1783 (1974)

Chaouche, M., and Koch, D. L. "Rheology of non-Brownian rigid fiber suspensions with adhesive contacts". J. Rheol. **45**, 369-382 (2001).

Donev A., I. Cisse, D. Sachs, E. A. Variano, F. H. Stillinger, R. Connelly, S. Torquato, P. M. Chaikin, "Improving the Density of Jammed Disordered Packings Using Ellipsoids", Science 303, 990-993 (2004).

Happel J. and H. Brenner, "*Low Reynolds number hydrodynamics*" (Martinus Nijhoff Publishers, The Hague, 1983)

Jeffery, G. B. "The motion of ellipsoidal particles immersed in a viscous fluid". Proc. Royal Soc. London A **102**, 161-179 (1922).

Keshtkar M., MC Heuzey, and PJ Carreau. "Rheological behavior of fiber-filled model suspensions: effect of fiber flexibility," J. Rheology **53**, 631–650 (2009).

Khalkhal, F., P. J. Carreau, and G. Ausias, Effect of flow history on linear viscoelastic properties and the evolution of the structure of multiwalled carbon nanotube suspensions in

an epoxy. J. Rheol. **55**, 153-175 (2011).

Larson R. G., "*The Structure and Rheology of Complex Fluids*" (Oxford University Press, 1999).

Leal, L. G., and Hinch, E. J. "The effect of weak Brownian rotations on particles in shear flow," J. Fluid. Mech. **46**, 685-703 (1971).

Lindström, S. B., and Uesaka, T. A., "Numerical investigation of the rheology of sheared fiber suspensions", Phys. Fluids **21**, 083301 (2009).

Macosko, Ch. W., "*Rheology: Principles, Measurements, and Applications*" (Wiley-VCH, Inc., New York, 1994)

McCoy D. H., and M. M. Denn, "Secondary flow in a parallel plate rheometer," Rheol. Acta **10**, 408-411 (1971).

Mueller, S., Llewellin, E. W., and Mader, H. M. "The rheology of suspensions of solid particles." Proc. Royal Soc. London A **466**, 1201-1228 (2009).

Russell, W. B., D. A. Saville, and W. R. Schowalter, "*Colloidal dispersions" (*Cambridge University Press, Cambrige, 1989)

Solomon, M. J., and Spicer, P. T. "Microstructural regimes of colloidal rod suspensions, gels, and glasses." Soft Matter **6**, 1391-1400 (2010).

Switzer III L. H. and D. J. Klingenberg, "Rheology of sheared flexible fiber suspensions via fiber-level simulations", J. Rheol. **47**, 759-778 (2003)

Tillmark N. and P.H. Alfredsson, "Experiments on transition in plane Couette flow", J.Fluid. Mech. **235**, 89-102 (1992).

Van de Ven, T. G. M., "*Colloidal Hydrodynamics*" (Academic, London, 1989).